

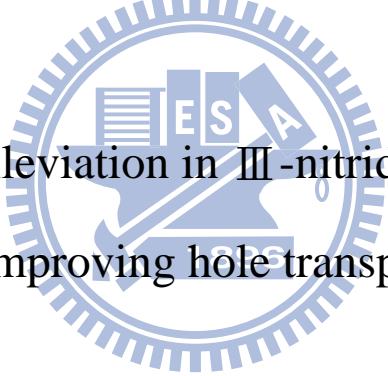
國立交通大學
電子物理研究所

碩士論文

改善電洞傳導行為緩解III族氮化物發光二極體效率

下降特性之研究

Efficiency droop alleviation in III-nitride light-emitting diodes
by improving hole transportation



研究生：張瑋婷

指導教授：郭浩中 教授

林烜輝 教授

中華民國一百年三月

改善電洞傳導行為緩解III族氮化物發光二極體效率下降特性之研究

Efficiency droop alleviation in III-nitride light-emitting diodes by improving
hole transportation

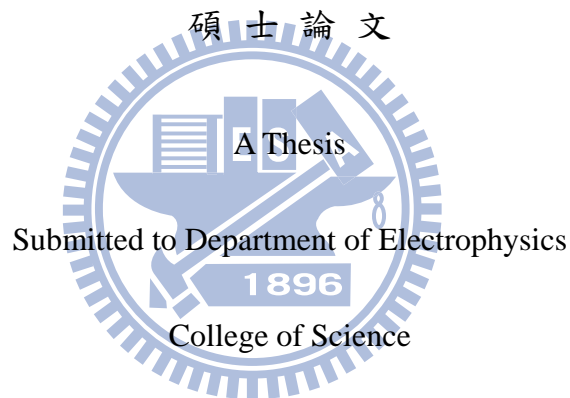
研究生：張瑋婷

Student：Wei-Ting Chang

指導教授：郭浩中 教授
林烜輝 教授

Advisor：Prof. Hao-Chung Kuo
Prof. Shiuan-Huei Lin

國立交通大學
電子物理系
碩士論文



National Chiao Tung University

in Partial Fulfillment of the Requirements

for the Degree of Master

in

Electrophysics

March 2011

Hsinchu, Taiwan, Republic of China

中華民國一百年三月

改善電洞傳導行為緩解III族氮化物發光二極體效率下降特性之研究

研究生：張瑋婷

指導教授：郭浩中教授

林烜輝教授

國立交通大學電子物理系碩士班

摘要

本論文中，我們針對為傳統氮化鎵發光二極體的磊晶結構進行改良，改善電洞傳導行為以緩解三族氮化物發光二極體效率隨外加電流提高而驟降之問題。

第一部分設計漸變鋁含量的氮化鋁鎵電子阻擋層，期待除了強化阻擋電子溢流外，更可增加電洞注入效率，藉以提升主動層載子複合發光效率，在以理論分析找得最佳化設計後，實作樣品利用電激發螢光(Electroluminescence, EL)量測，驗證其發光強度確實相較於使用傳統電子阻擋層之元件為佳，並且緩解了發光效率在高電流會產生效率驟降的情況。

再者，我們在使用氮化鎵作為主動層量子井的紫外光(UV) LED 中，將位能障材料氮化鋁鎵替換成氮化鋁鎵鎵，量測證實其與三元材料晶格常數和能隙相近的四元材料，有較好的磊晶品質外，EL 量測結果也顯示其突出的電特性與發光效率。由於四元材料可以經由調整鋁和鎵的含量而自由變動其晶格常數、能隙、應力、和載子侷限效果，因此在藉由理論模擬分析後，我們推論使用氮化鋁鎵鎵作為位能障，可以提高量子井中電子的侷限、電洞的傳導與載子的遷移率，因而改善 LED 效率驟降的問題。

Efficiency droop alleviation in III-nitride light-emitting diodes by improving hole transportation

Student : Wei-Ting Chang

Advisor: Prof. Hao-Chung Kuo

Prof. Shiuan-Huei Lin

Department of Electrophysics
National Chiao Tung University

Abstract

In this thesis, we designed the epitaxial structure of InGaN light-emitting diodes (LEDs) to improve the transportation of holes, which leads to reduction of efficiency droop.

We first designed a graded-composition electron blocking layer (GEBL) for c-plane InGaN/GaN LEDs. The simulation results demonstrated that such GEBL can effectively enhance the capability of hole transportation across the EBL as well as the electron confinement. Consequently, the LED with GEBL grown by metal-organic chemical vapor deposition exhibited lower forward voltage and series resistance, and much higher output power at high current density, as compared to conventional LED.

Second, we demonstrated InGaN-based UV LEDs with AlGaN and InAlGaN barrier. EL results indicate that the light output performance could be enhanced effectively when replacing the conventional AlGaN barriers by InAlGaN barriers. Furthermore, from numerical analysis, it is believed that InGaN/AlInGaN MQWs exhibit higher radiative recombination rate and low efficiency droop at a high injection current because of the better band-offset ratio and the higher hole mobility, which leads to the uniform distribution of holes in the active region.

誌謝

很難相信兩年研究生涯會過得如此的快，直到現在還是覺得要畢業了很不真實。想想這段時間裡過得非常充實，除了學術上知識的吸收外，也在實驗室中交到了許多好朋友，使我有個多姿多采的碩班生活。在此，要感謝在這兩年中幫助、陪伴我成長的人，使我可以順利完成我的碩士學位。

首先，我要感謝林烜輝老師和郭浩中老師的指導，謝謝老師提供了很好的研究環境，還有平時對我的幫助與鼓勵，使我能夠有許多想法去解決研究上所遇到的問題。

感謝在我初進實驗室，帶著我學習的清華學長、閔安學長、小柯學長、與永吉學長，使我熟習到理論知識與實驗技術，紮根了我 LED 研究的基礎。再來要感謝的是 Joseph 學長的照顧，對於我研究上的規劃幫助許多，除了 Meeting 上的指導，平常總是不厭其煩的替我解答與給予建言，使我得以順利完成碩班研究。感謝李博學長、金釵學姐、與鏡學學長，對於我在報告時提供不少想法與建議，令我收穫良多。感謝士邦學長與涂學長，有你們的幫助我才能得到穩定的樣品完成研究。感謝總是很可靠的小昕學長，不管是實驗與研究上的教導，還是私下的鼓勵與叮嚀，使我能有所成長。感謝羿蓁、大寶、Jolin、肉圓、幼慶、小杜、家齊、阿 po、祐國、Just、SGG、等碩二的同學們，因為有你們使我的碩班生活增添不少快樂回憶，我會永遠記得那些揪團吃飯或是出遊的時光，一起分享歡笑與宣洩壓力，很開心可以認識到可愛的大家。感謝 Bush 學弟，量測變溫 EL 有你協助輕鬆許多，能有你這麼聰明、負責的學弟真的很幸運，也祝福你能在未來一年的順利完成研究、順利畢業。

最後要感謝我最最親愛的家人，感謝爸媽一直以來對我的支持與關愛，使我可以安心的完成學業，謝謝你們！

Content

| | |
|----------------------|-----|
| 摘要..... | i |
| Abstract..... | ii |
| 誌謝..... | iii |
| Content..... | iv |
| List of Tables..... | vi |
| List of Figures..... | vii |

Chapter 1 Introduction

| | |
|---|---|
| 1.1 Bandgaps of group III-nitride materials..... | 1 |
| 1.2 InGaN-based Light-Emitting Diodes (LEDs)..... | 2 |
| 1.3 Motivation..... | 4 |

Chapter 2 Properties of III-Nitride semiconductor

| | |
|---|----|
| 2.1 Theory of radiative recombination and LED efficiency..... | 6 |
| 2.2 The basic concept of efficiency droop..... | 9 |
| 2.3 The mismatch of the charge carrier in III-nitride LEDs..... | 11 |
| 2.4 The pros and cons of inserting electron blocking layer (EBL) in III-nitride LEDs..... | 13 |

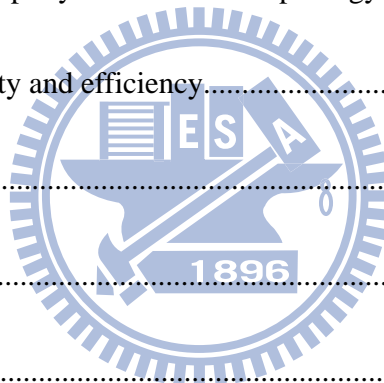
Chapter 3 Experimental instrument and numerical simulation

| | |
|--|----|
| 3.1 Electroluminescence (EL) measurement..... | 15 |
| 3.2 Physical models and parameter setting..... | 16 |

Chapter 4 Study of InGaN LEDs with graded-composition EBL

| | |
|---|----|
| 4.1 Introduction..... | 26 |
| 4.2 Simulation structure and parameter setting..... | 28 |

| | |
|--|-----------|
| 4.3 Calculated band diagrams and carrier distribution analysis..... | 30 |
| 4.4 Sample structure and Fabrication..... | 35 |
| 4.5 Analysis of current-dependence EL characteristics and efficiency droop behavior..... | 37 |
| 4.6 Summary..... | 39 |
| Chapter 5 Study of InGaN-Based UV LEDs with InAlGaN Barrier | |
| 5.1 Introduction..... | 41 |
| 5.2 Sample structure and fabrication..... | 43 |
| 5.3 Investigation of optical property and surface morphology..... | 45 |
| 5.4 Current-dependent intensity and efficiency..... | 47 |
| 5.5 Theoretical analysis..... | 50 |
| 5.6 Summary..... | 55 |
| Chapter 6 Conclusion..... | 56 |
| Reference..... | 58 |



List of Tables

| | | |
|-----------|---|----|
| Table 3.1 | Material parameters of the binary semiconductors GaN, AlN, and InN at room temperature..... | 19 |
| Table 3.2 | Bandgap energy of GaN, AlN and InN related-temperature parameters..... | 21 |
| Table 3.3 | Mobility parameters of GaN, AlN and InN..... | 25 |
| Table 5.1 | Simulation parameters in band-offset ratio and carrier mobility..... | 53 |



List of Figures

| | | |
|--------------|---|----|
| Figure 1.1 | Bandgap energy versus lattice constant of III-V nitride semiconductors at room temperature..... | 1 |
| Figure 1.2 | The schematic drawing of InGaN LED..... | 3 |
| Figure 2.1.1 | Illustration of radiative and non-radiative transition in a semiconductor..... | 6 |
| Figure 2.2.1 | Efficiency droop of LEDs..... | 10 |
| Figure 2.3.1 | Carrier transportation and recombination behavior in MQWs..... | 12 |
| Figure 2.4.1 | Calculated band diagrams of InGaN/GaN LEDs with Al _{0.32} Ga _{0.68} N EBL at 90 A/cm ² | 14 |
| Figure 2.4.2 | IQE and leakage current ratio of GaInN/GaN and GaInN/AlGaInN LEDs with and without polarization effect in the MQW and/or the EBL..... | 14 |
| Figure 3.1.1 | The schematic of electroluminescence setup..... | 15 |
| Figure 3.1.2 | The photograph of electroluminescence measure system..... | 16 |
| Figure 4.1 | (a) The influence of inserting EBL between MQWs and p-GaN (b) Schematic diagram of the concept of band engineering at EBL..... | 27 |
| Figure 4.2.1 | The simulation structure of GEBL LEDs with material, thickness, and doping concentration..... | 29 |
| Figure 4.2.2 | The simulation structure of conventional LED, LED A, B, and C..... | 29 |
| Figure 4.3.1 | Calculated energy band diagrams of (a) Al ₀ GaN to Al _{0.15} Ga _{0.85} N, (b) Al ₀ GaN to Al _{0.25} Ga _{0.75} N, and (c) Al ₀ GaN to Al _{0.35} Ga _{0.65} N graded-composition EBLs at a current density of 100 A/cm ² | 30 |
| Figure 4.3.2 | The calculated band diagram of GEBL LEDs at 20, 100, and 300 A/cm ² ... | 31 |
| Figure 4.3.3 | Simulated electron current density for conventional LEDs and GEBL LEDs..... | 33 |
| Figure 4.3.4 | Distribution of hole concentration of conventional LEDs and GEBL LEDs..... | 33 |
| Figure 4.3.5 | Calculated (a) hole concentration distribution and (b) electron concentration distribution of conventional and GEBL LEDs at a current density of 100 A/cm ² | 34 |

| | | |
|--------------|---|----|
| Figure 4.4.1 | The schematic drawing of sample structure (GEBL LED)..... | 36 |
| Figure 4.4.2 | The schematic drawing of fabrication processes of LED..... | 36 |
| Figure 4.5.1 | Forward voltage and output power as a function of current density for conventional and GEBL LEDs..... | 38 |
| Figure 4.5.2 | Normalized efficiency as a function of current density for conventional and GEBL LEDs..... | 39 |
| Figure 5.1.1 | Calculated band diagram of reference GaInN/GaN LED as well as AlGaInN LED structure with polarization-matched MQW under a forward bias condition..... | 42 |
| Figure 5.1.2 | Normalized EQE as a function of forward current density for GaInN/AlGaInN MQW LEDs and reference GaInN/GaN MQW LEDs..... | 43 |
| Figure 5.2 | The schematic drawing of sample structure (UV LED)..... | 44 |
| Figure 5.3.1 | Room-temperature PL spectra of AlGaIn and InAlGaIn bulks. Insert Figs. shows surface morphology AFM over $5 \times 5 \mu\text{m}^2$ of bulk AlGaIn (RMS:0.813 nm) and InAlGaIn (RMS:0.595 nm) layer with thickness about 50 nm..... | 46 |
| Figure 5.3.2 | (a)HRXRD (ω -2 θ) curves in the (002) reflections of InGaIn/AlGaIn and InGaIn/InAlGaIn MQW. Cross-sectional TEM images of (b) InGaIn/AlGaIn and (c) InGaIn/InAlGaIn MQW. The diffraction condition is g0002..... | 47 |
| Figure 5.4 | (a) L-I-V curves of the LEDs with AlGaIn (dash) and InAlGaIn (solid) barrier. (b) Normalized Efficiency curves of experimental. Insert in Fig. 5.4(a) shows the mesa-type UV chips..... | 49 |
| Figure 5.5.1 | Simulation results of normalized IQE under different carrier mobility..... | 51 |
| Figure 5.5.2 | Simulation results of normalized IQE under different band offset ratio..... | 52 |
| Figure 5.5.3 | Normalized Efficiency curves of experimental and simulated..... | 54 |
| Figure 5.5.4 | Distribution of (a) Electron (b) Hole concentrations, and (c) Radiative recombination rates concentrations of the LEDs with AlGaIn and InAlGaIn barrier under a high forward current density of 100 A/cm^2 | 54 |

Chapter 1 Introduction

1.1 Bandgaps of group III-Nitride materials

In recent decades, the III-Nitrides materials (InN, GaN, and AlN related alloys) become an interesting class of wide bandgap materials and play an important role in semiconductor devices. The bandgap of the wurtzite polytypes of III-nitrides material cover a very wide range, from 0.7 eV for InN to 6.1 eV for AlN, which represents the emission wavelength from infrared (IR) region to deep ultraviolet (UV). Fig. 1.1 shows the bandgaps of various alloys of III-Nitrides.

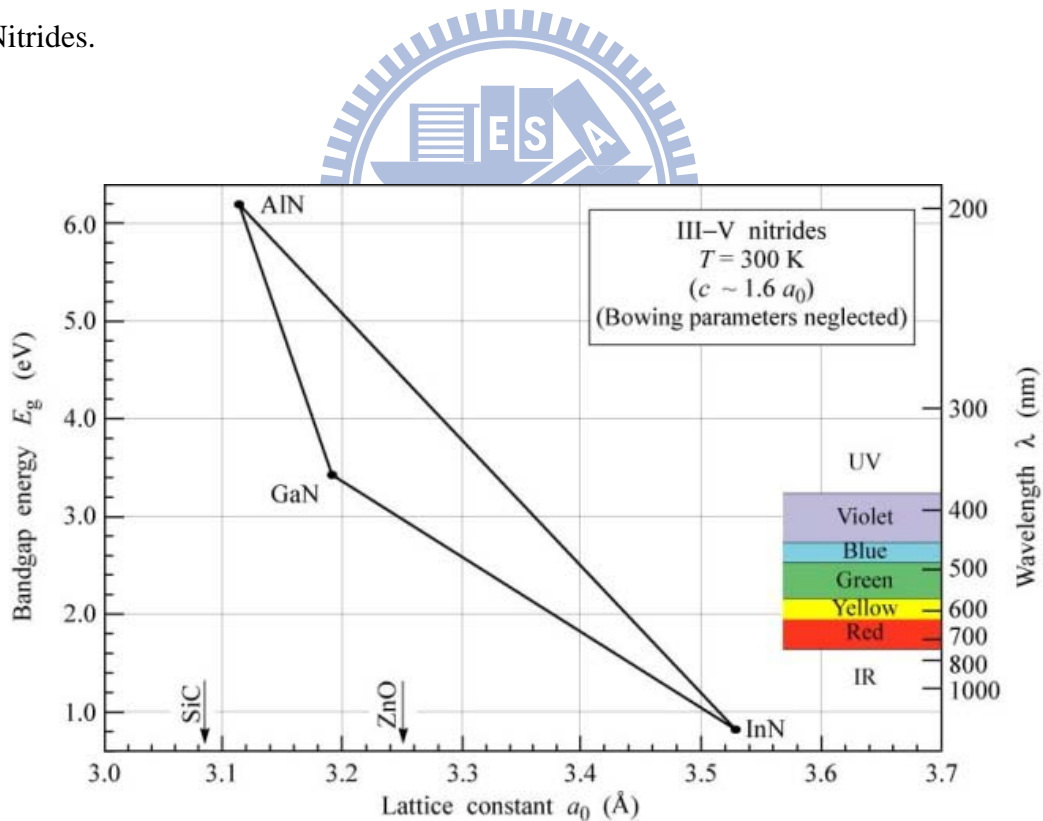


Fig. 1.1 Bandgap energy versus lattice constant of III-V nitride semiconductors at room temperature. [1]

This wide emission wavelength range makes it promising for applying in the applications of optoelectronic devices. By using III-Nitride with different alloy compositions, we can get a material with the desired bandgap. This phenomenon is quite different from other III-V materials systems based on GaAs, AlAs, InAs, GaP and related alloys. In addition, the III-Nitrides materials are expected to be superior to the counterparts made of Si and other III-V materials for high-temperature and high-power applications [2-5].

1.2 GaN-based LEDs

Light Emitting Diodes (LEDs) are solid state devices which emit light when electrical current passes through them. In LEDs made of semiconductors, the color of the light depends on the bandgap of the semiconductor material, proceeding from red through orange, yellow, green, blue and violet as the gap increases.

The first blue light-emitting diode (LED) using III-Nitrides materials was fabricated by J. I. Pankove *et al.* [6] with an metal-i-n structure in 1972. Since that, related research is going on continually. However, progresses have been limited because of highly background *n*-type concentration resulting from the native defects commonly thought to be nitrogen vacancies and residual impurities such as Si and oxygen acted as an efficient donor, poorly conducting *p*-type GaN, and the lack of appropriate substrates for epitaxial growth. Until late 1980s, H. Amano *et al.* [7, 8] discovered a very useful application of a low-temperature buffer layer and

developed low-energy electron beam interaction (LEEBI) techniques to obtain better GaN epilayer and conductive *p*-type GaN, initiated a new strong interest in this research field. Finally, the first GaN-based blue LED constructed of a real *p*-*n* junction was achieved, which had greatly improved in the device performance. However, the acceptor concentration of *p*-type GaN is still too low such that the application of these materials is still unreliable. After that, in 1992, S. Nakamura *et al.* [9] achieved better conductive *p*-type GaN material by introducing a simple thermal annealing procedure in nitrogen ambient ($\geq 750\text{ }^{\circ}\text{C}$). Afterward Nakamura and Mukai [10] succeeded in growing high-quality InGaN films that emitted strong band-to-band emission from green to UV by changing the indium content of InGaN with a two-flow MOCVD method. Nowadays, Most of III-Nitride based light emitting devices uses InGaN as active layer instead of GaN because the difficulty of fabricating high efficiency GaN based light emitting devices. Adding a small amount of indium into the GaN is very important to obtain a strong band-to-band emission at RT. The based design of GaN LEDs is shown in Fig. 1.2.

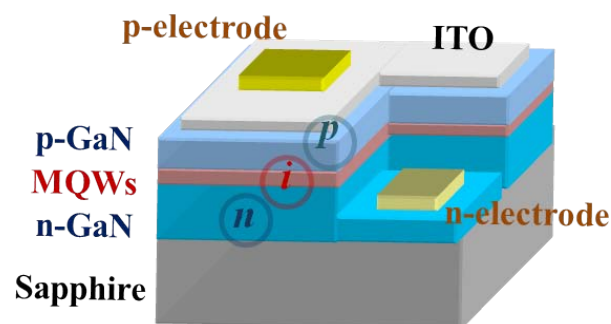


Fig. 1.2 The schematic drawing of InGaN LED

1.3 Motivation

Solid-state lighting offers much potential to save energy and enhance the quality of our building environments, especially refers to GaN-based LEDs. However, for the high efficiency lighting devices, III-nitride semiconductors have some inherent drawbacks to deteriorate the lighting efficiency. This phenomenon which known as efficiency droop is a severe limitation for high power devices that operate at high current densities and must be overcome to enable the LEDs needed for solid-state general illumination. The efficiency droop is caused by a nonradiative carrier loss mechanism, which is small at low currents but becomes significant for high injection currents. Competition between radiative recombination and this droop-causing mechanism results in the reduction in efficiency as current increases. The physical origin of efficiency droop remains controversial, and several different mechanisms have been suggested as explanations, including carrier leakage from the active region [11]. Auger recombination [12], junction heating [13], and carrier delocalization from In-rich low-defect-density regions at high carrier densities [14]. Carrier leakage in InGaN LEDs generally refers to the escape of electrons from the active region to the p-type region. These leakage electrons may then recombine with holes either in the p-type region or at the contacts, dominantly by nonradiative processes. Therefore, fewer holes than electrons are injected into the active region. These two phenomena that escape of electrons from the active region and reduced hole concentration of any carrier leakage explanation for droop. Hole injected into the active region may be the limiting factor,

possibly due to the low p-type doping efficiency or the electron blocking layer (EBL) acting as a potential barrier also for holes. As a result of the low hole injection, current across the device is dominated by electrons. Devices with p-type active regions which should increase hole injection efficiency have been proposed as a solution to this problem.

For this thesis, we investigated the injection current dependence EL intensity at room temperature. Then we discussed the normalized efficiency as a function of injection current density at room temperature clearly and used APSYS simulation to make sure our model is correct, so the physical mechanisms of current dependent efficiency of InGaN/GaN LED has been confirmed.

This thesis is organized in the following way: In chapter 2, we give some theoretical backgrounds and characteristics about InGaN MQW structures. The experimental setups and theory model are stated in chapter 3. In chapter 4, we present the simulation and experiment results and discuss for optical and electrical properties of InGaN/GaN MQW LED with graded composition electron blocking layer. In chapter 5, we show the experiment results and discuss for physical mechanisms of quaternary barrier MQW as a function of injection current density in InGaN/AlInGaN LEDs. Finally, we gave a brief summary of the study in chapter 6.

Chapter 2 Properties of III-Nitride semiconductor

2.1 Theory of radiative recombination and LED efficiency

LEDs are a class of diode that emit spontaneous radiation under suitable forward bias condition. Injection electroluminescence (EL) is most important mechanism for exciting the semiconductor material. Under forward bias conditions, both electrons from n-type semiconductor and holes from p-type semiconductor all inject to active region and then recombine either, and accompany by the emission of a photon (radiatively) or non-radiatively. This two recombination pathways can be considered as parallel processes occurring across the bandgap of the active region material, as illustrated in Fig. 2.1.1. If the radiative lifetime is denoted as τ_r and the non-radiative lifetime is denoted as τ_{nr} , then the total probability of recombination is given by the sum of the radiative and non-radiative probability:

$$\frac{1}{\tau} = \frac{1}{\tau_r} + \frac{1}{\tau_{nr}} \quad (2.1.1)$$

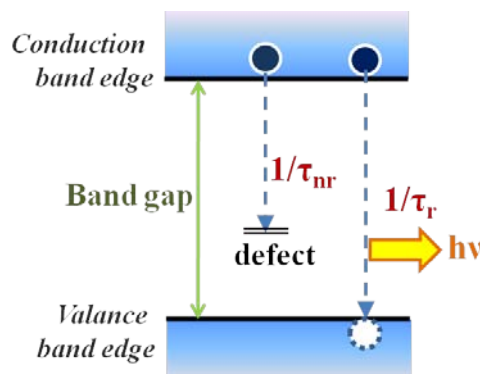


Fig. 2.1.1 Illustration of radiative and non-radiative transition in a semiconductor.

The relative probability of radiative recombination is given by the radiative probability

over the total probability of recombination. Therefore, the internal quantum efficiency (IQE) can be expressed in terms of the radiative and non-radiative lifetimes.

$$\eta_{\text{int}} = \frac{\tau_r^{-1}}{\tau_r^{-1} + \tau_{nr}^{-1}} \quad (2.1.2)$$

The IQE value of ideal active region of an LED is unity. From the concept of electrical excitation mechanism, the internal quantum efficiency is defined as:

$$\eta_{\text{int}} = \frac{\text{number of photons emitted from active region per second}}{\text{number of electrons injected into LED per second}} = \frac{P_{\text{int}}/h\nu}{I/e} \quad (2.1.3)$$

where P_{int} is the optical power emitted from the active region and I is the injection current.

Photons emitted by the active region should escape from the LED die. In an ideal LED, all photons emitted by the active region are also emitted into free space. Such an LED has unity extraction efficiency. However, in a real LED, not all the power emitted from the active region is emitted into free space. Some photons may never emit into the free space. This is due to several possible loss mechanisms. For example, light may be reabsorbed by material itself of the LED. Light may be incident on a metallic contact surface and be absorbed by the metal. In addition, the phenomenon of the total internal reflection, also referred to as the trapped light phenomenon, reduces the ability of light to escape from the active region.

The extraction efficiency can be a severe limitation for high performance LEDs. It is quite difficult to increase the extraction efficiency beyond 50% without resorting to high

sophisticated and costly device processes. The light extraction efficiency (LEE) is defined as:

$$\eta_{\text{int}} = \frac{\text{number of photons emitted into free space per second}}{\text{number of photons emitted from active region per second}} = \frac{P/h\nu}{P_{\text{int}}/h\nu} \quad (2.1.4)$$

where P is the optical power emitted into free space. Considering the refractive indices of GaN ($n = 2.5$) and air, for the light escape cone, is about 23% due to the critical angle.

Assuming that light emitted from sidewalls and backside is neglected, one expects that approximately only 4% of the internal light can be extracted from a surface.

The light outside the escape cone is reflected into the substrate and is repeatedly reflected, then reabsorbed by active layers or electrodes, unless it escapes through the sidewalls. However, there is much room for improvement of the light extraction efficiency. For example, roughening of the top LED surface increased the light extraction efficiency.

Finally, the external quantum efficiency (EQE) is defined as:

$$\eta_{\text{ext}} = \frac{\text{number of photons emitted into free space per second}}{\text{number of electrons injected into LED per second}} = \frac{P/h\nu}{I/e}$$

$$\eta_{\text{ext}} = \eta_{\text{int}}\eta_{\text{extraction}} \quad (2.1.5)$$

from the above equation, we can know that the EQE depend on IQE and LEE, therefore, the improvement of IQE and LEE pay an important role of LED. Recently, the patterned sapphire substrate is introduced to improve the IQE which is attributed to reduce the

dislocation density and enhance the LEE due light emit to substrate may reflect and emit into free space.

2.2 The basic concept of efficiency droop

Solid-state lightings, especially InGaN/GaN light-emitting diodes (LEDs), have been vigorously developed to take the place of traditional lighting source, due to its potentially higher efficiency. It is imperative that LEDs produce high luminous flux which necessitates high efficiency at high current densities. However, as the efficiency of LEDs increasing, the upcoming challenge is the efficiency “droop” for high-power applications [15]. The external quantum efficiency EQE reaches its peak at current densities as low as 10 A/cm^2 and monotonically decreases with further increase in current, as illustrated in Fig. 2.2.1. It means that the efficiency reduces rapidly when LED operating under high carrier density.

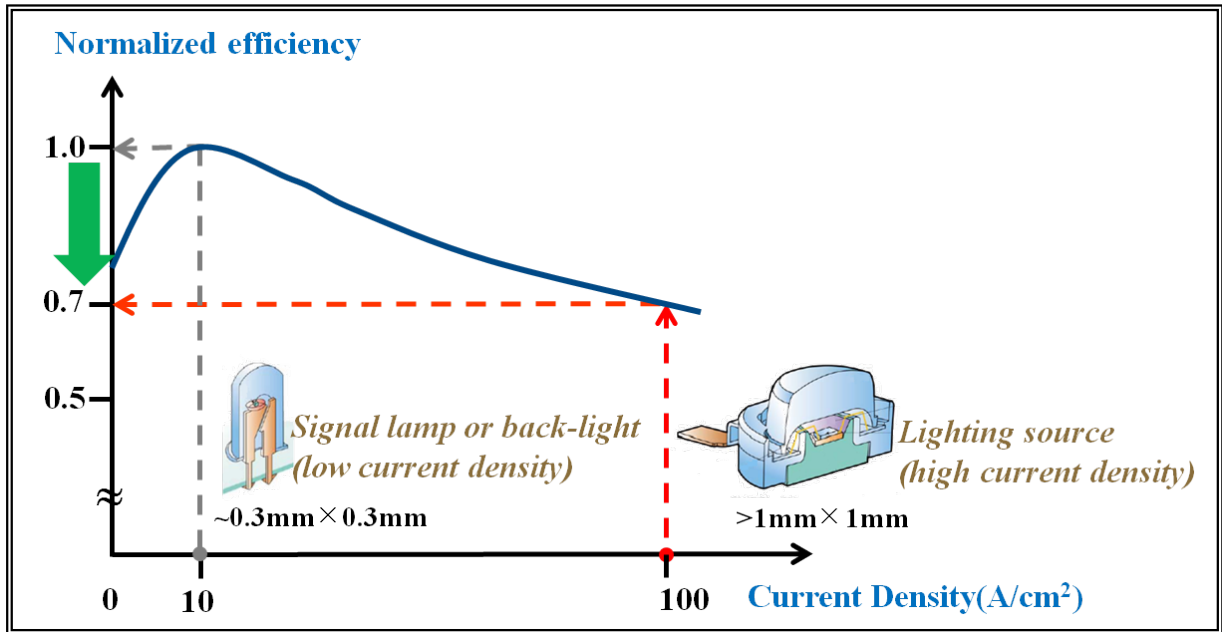


Fig. 2.2.1 Efficiency droop of LEDs

Contrary to what may appear at an instant glance, dislocations have been shown to reduce the overall efficiency but not affect the efficiency droop. The major cause of efficiency droop is still a huge controversy. Various possible mechanisms of droop including carrier overflow [16], non-uniform distribution of holes [17, 18], Auger scattering [19], carrier delocalization [20], junction heating have been proposed, but the genesis of the efficiency droop is still the topic of an active debate. Although Auger recombination was proposed for the efficiency droop,[21]the Auger losses in such a wide bandgap semiconductor are expected to be very small,[22] which has also been verified using fully microscopic many body models.[23] In addition, if an inherent process such as Auger recombination were solely responsible for the efficiency degradation, this would have

undoubtedly prevented laser action, which requires high injection levels, in InGaN which is not the case. The efficiency droop was also noted to be related to the quantum well thickness in the form of peak efficiency shifting to higher injection currents with increasing well thickness.[24] It was suggested that the effect of polarization field may be playing a role.[25] The observations, however, are consistent with large effective mass of holes because of which it is very likely that only the first QW next to the p-barrier substantially contributes to radiative recombination. Making the well wider, therefore, increases the emission intensity providing that the layer quality can be maintained. It has also been suggested that in wider QWs the carrier density is reduced for the same injection level and thus reduced Auger recombination.[25] What is very revealing is that in below barrier photoexcitation experiments (photons absorbed only in the QWs), where carriers are excited and recombined in the QWs only, the efficiency droop was not observed at carrier generation rates comparable to electrical injection which indicates that efficiency droop is related to the carrier injection, transport, and leakage processes.[25]

2.3 The mismatch of the charge carrier in III-nitride LEDs

The transportation behavior of electrons and holes in III-nitride are known to be substantially different. The high effective mass of holes in GaN ($1.1m_0$, compared to $0.2m_0$ for electrons) and the resulting low mobility make hole injection into the lower lying QWs

(near p-side layer) difficult. On the other hand, high electron concentrations are achievable with the n-type dopant Si due to its relatively low ionization energy of about 20 meV,[26] and electron mobility is fairly high, with values above $200 \text{ cm}^2 \text{ V}^{-1} \text{ s}^{-1}$ being typical for n-type GaN. By contrast, high hole concentrations are generally not achievable due to the large ionization energy of the p-type dopant Mg in GaN, which has been estimated at 120 meV.[27] In addition, hole mobility is typically on the order of $10 \text{ cm}^2 \text{ V}^{-1} \text{ s}^{-1}$ for doped p-type GaN.[28] Furthermore, due to poor hole transport, the radiatively recombination distribution in MQWs come to be non-uniform and gather in nearest p-side wells, as illustrated in Fig. 2.3.1. Then, in high current injection, this mismatch of the charge carrier could also produce electron overflow or auger recombination and be one of origins for efficiency droop.

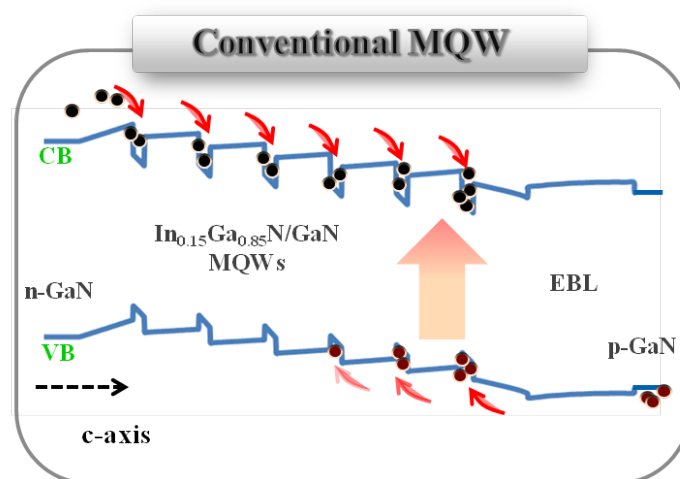
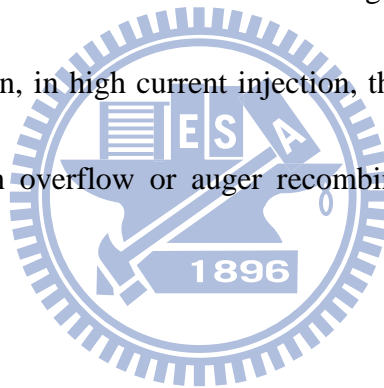


Fig. 2.3.1 Carrier transportation and recombination behavior in MQWs.

2.4 The pros and cons of inserting electron blocking layer in III-nitride LEDs

Carrier overflow out of the active region as well as inefficient injection and transportation of holes have been identified to be the major reasons of efficiency droop.[18, 30] To reduce the carrier overflow, an $\text{Al}_x\text{Ga}_{1-x}\text{N}$ electron blocking layer (so called EBL) was adopted in common InGaN LED structures. However, it has been reported that the large polarization field in $\text{Al}_x\text{Ga}_{1-x}\text{N}$ EBL reduces the effective barrier height for electrons, as shown in Fig. 2.4.1.[32] Therefore, the carrier overflow cannot be suppressed effectively. On the other hand, the polarization-field induced band bending and the valence band offset (ΔE_v) at the interfaces of GaN and EBL are considered to retard the injection of holes.[31, 32] To reduce the polarization field in EBL, the polarization-matched EBLs (AlInN or AlInGaN) were proposed and demonstrated to be more effective in electron confinement.[33, 34] However, it has difficulties of realization in epitaxy, and the crystal quality of the subsequent p-GaN layer will be degraded. Most importantly, the hole injection cannot be improved effectively due to the existence of the ΔE_v between the last GaN barrier and the EBL.[32]

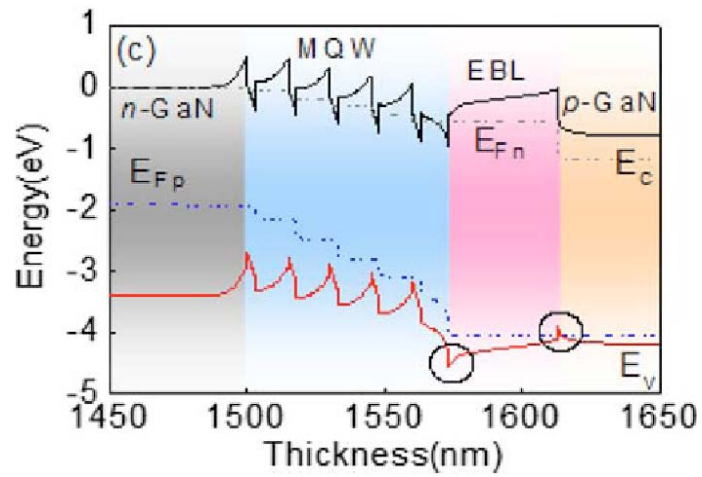


Fig 2.4.1 Calculated band diagrams of InGaN/GaN LEDs with $\text{Al}_{0.32}\text{Ga}_{0.68}\text{N}$ EBL at 90 A/cm^2 [32].

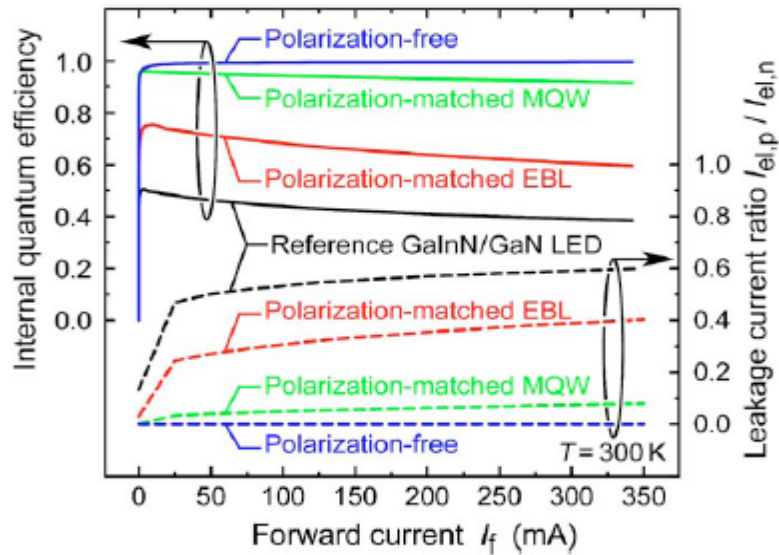


Fig 2.4.2 IQE and leakage current ratio of GaInN/GaN and GaInN/AlGaInN LEDs with and without polarization effect in the MQW and/or the EBL. [31]

Chapter 3 Experimental instrument and numerical simulation

3.1 Electroluminescence (EL)

Fig. 3.1.1 shows the schematic of electroluminescence measurement systems. A set of instruments including CW current source Kiethley 238, a microscope to observe the patterned electrode of sample surface, three axial stages for probe and fiber to detected the light output, and then the light detected by a 0.32 m monochromator (Jobin-Yvon Triax-320) with 1800, 1200, and 300 grooves/mm grating and the maximum width if the entrance slit was 1 mm. Figure B shows the photograph of electroluminescence measure system.

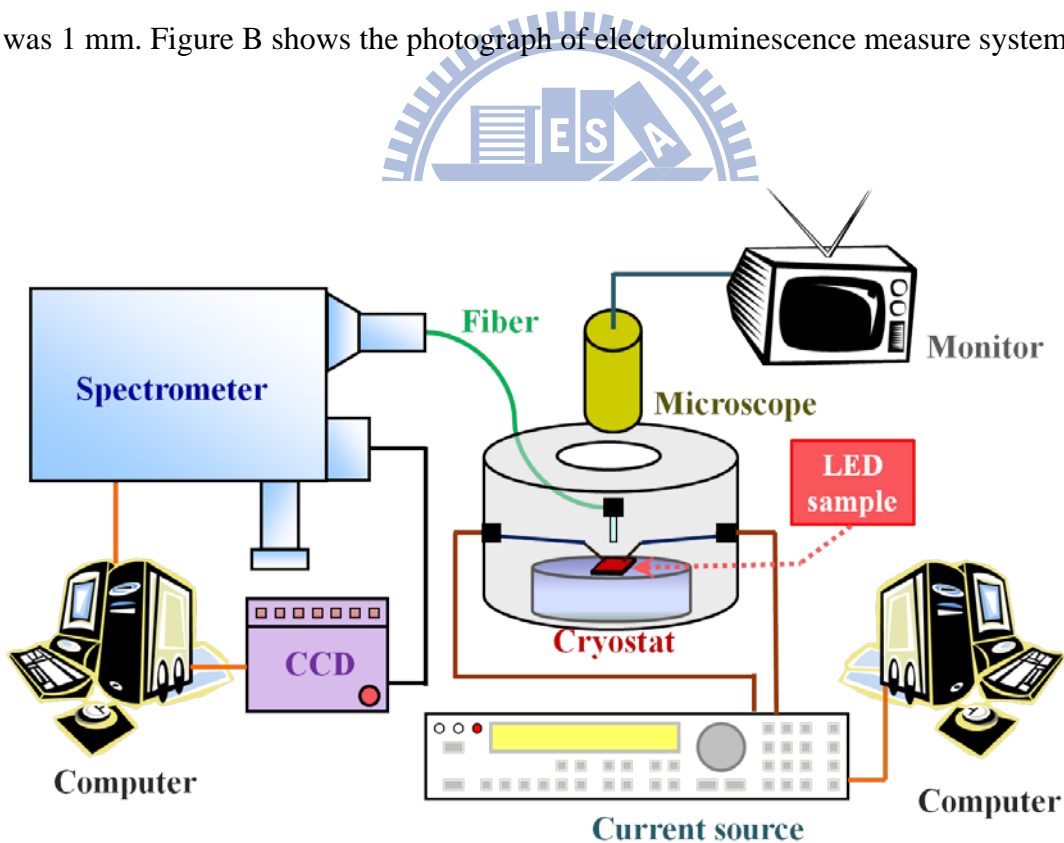


Fig. 3.1.1 The schematic of electroluminescence setup.

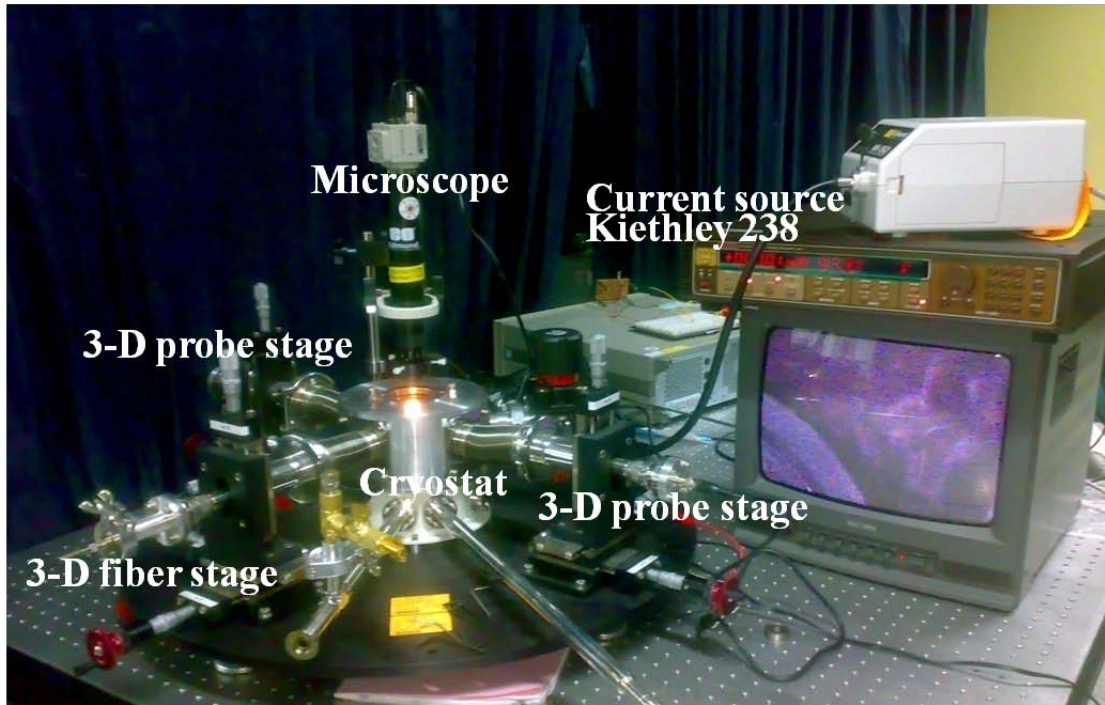


Fig. 3.1.2 The photograph of electroluminescence measure system.

3.2 Physical models and parameter setting

To explore theoretically this study, the numerical simulation software, APSYS (Advanced Physical Models of Semiconductor Devices), was used to preview and optimize our LEDs design, and it is based on 2D/3D finite element analysis of electrical, optical and thermal properties of compound semiconductor devices. Emphasis is placed on band structure engineering and quantum mechanical effects. Inclusion of various optical modules also makes this simulation package attractive for applications involving photosensitive or light emitting devices. The APSYS simulator solves the Poisson's equation, the current continuity equations, the carrier transport equations, the quantum mechanical wave equation,

and the heat transfer equations, via self-consistent manner. Built-in polarization induced by spontaneous and piezoelectric polarization is considered at hetero-interfaces of nitride related devices. We put commonly accepted physical parameters to perform the simulations. Usually, for performing a simulation, the used material parameters had been set as default data from former research results. However, we also can modify and update these values to be similar to real device. Therefore, setting suitable parameters for simulation is an important point.

3.2.1 Theoretical model

The physical model of the InGaN MQWs is considered in such a way that the conduction bands are assumed to be decoupled from valence subbands and have isotropic parabolic bands due to the larger bandgap of nitride semiconductor and the valence band structures, which includes the coupling of the heavy-hole (HH), the light-hole (LH), and the spin-orbit split-off bands, are calculated by the 6×6 Hamiltonian with envelop function approximation. By using the basis transformation, the 6×6 Hamiltonian can be transformed into a block-diagonalized Hamiltonian [35],

$$H_{6 \times 6} = \begin{bmatrix} H^U & 0 \\ 0 & H^L \end{bmatrix}$$

$$\text{with } H^U = \begin{bmatrix} F & K_t & -iH_t \\ K_t & G & \Delta - iH_t \\ iH_t & \Delta + iH_t & \lambda \end{bmatrix}, \quad H^L = \begin{bmatrix} F & K_t & iH_t \\ K_t & G & \Delta + iH_t \\ -iH_t & \Delta - iH_t & \lambda \end{bmatrix}$$

$$F = \Delta_1 + \Delta_2 + \lambda + \theta , G = \Delta_1 - \Delta_2 + \lambda + \theta$$

$$\lambda = \frac{\hbar^2}{2m_0} (A_1 k_z^2 + A_2 k_t^2) + \lambda_\varepsilon , \lambda_\varepsilon = D_1 \varepsilon_{zz} + D_1 (\varepsilon_{xx} + \varepsilon_{yy})$$

$$K_t = \frac{\hbar^2}{2m_0} A_5 k_t^2 , H_t = \frac{\hbar^2}{2m_0} A_6 k_z k_t$$

$$\Delta = \sqrt{2} \Delta_3 , \text{ and } k_t^2 = k_x^2 + k_y^2$$

where m_0 is the free electron mass. The A_i parameters are related to the hole effective masses. The crystal-field split energy is $\Delta_{cr} = \Delta_1$ and the spin-orbit splitting is $\Delta_{so} = 3\Delta_2 = 3\Delta_3$. The D_i parameters are deformation potential constants.

To obtain the numerical parameters required for calculations for the nitrogen-containing semiconductors, a linear interpolation between the parameters of the relevant binary semiconductors is utilized except for the unstrained bandgap energies. The material parameters of the binary semiconductors are taken from the paper by Vurgaftman and Meyer [36] and summarized in Table 3.1.

Table 3.1 Material parameters of the binary semiconductors GaN, AlN, and InN at room temperature. ($\Delta_{cr}=\Delta_I$, $\Delta_{so}=3\Delta_2=3\Delta_3$)

| Parameter | Symbol | GaN | AlN | InN |
|--|-----------------------|-------|--------|-------|
| Lattice constant | a_0 (Å) | 3.189 | 3.112 | 3.545 |
| Spin-orbit split energy | Δ_{so} (eV) | 0.017 | 0.019 | 0.005 |
| Crystal-field split energy | Δ_{cr} (meV/K) | 0.010 | -0.169 | 0.040 |
| Hole effective mass parameter | A_1 | -7.21 | -3.86 | -8.21 |
| | A_2 | -0.44 | -0.25 | -0.68 |
| | A_3 | 6.68 | 3.58 | 7.57 |
| | A_4 | -3.46 | -1.32 | -5.23 |
| | A_5 | -3.40 | -1.47 | -5.11 |
| | A_6 | -4.90 | -1.64 | -5.96 |
| Hydrost. deform. potential (<i>c</i> -axis) | a_z (eV) | -4.9 | -3.4 | -3.5 |
| Hydrost. deform. potential (transverse) | a_t (eV) | -11.3 | -11.8 | -3.5 |
| Shear deform. potential | D_1 (eV) | -3.7 | -17.1 | -3.7 |
| | D_2 (eV) | 4.5 | 7.9 | 4.5 |
| | D_3 (eV) | 8.2 | 8.8 | 8.2 |
| | D_4 (eV) | -4.1 | -3.9 | -4.1 |
| Elastic stiffness constant | c_{33} (GPa) | 398 | 373 | 224 |
| | c_{13} (GPa) | 106 | 108 | 92 |
| Hole effective mass (<i>c</i> -axis) | m_e^z/m_0 | 0.2 | 0.32 | 0.07 |
| Hole effective mass (transverse) | m_e^t/m_0 | 0.2 | 0.30 | 0.07 |

3.2.2 Bandgap energy of III-nitride Alloys

As being mentioned before, nitride-based materials are mainly made up of three binary compounds (GaN, AlN, and InN), so the bandgap energy of these nitride-based compounds is also made up of these binary materials. Besides, the bandgap energy of these three binary materials is related to the temperature. Therefore, we will extend this discussion to ternary and quaternary nitride-based compound in the next paragraph.

The bandgap energy of GaN, AlN, and InN at temperature T can be expressed by the Varshni formula (3.2.1) [37]

$$E_g(T) = E_g(0) - \frac{\alpha T^2}{T + \beta}$$

where $E_g(T)$ is the bandgap energy at temperature T , $E_g(0)$ is the bandgap energy at 0 K, α and β are material-related constant, of the binary alloys are listed in Table 3.2.[36]

The bandgap energy of $\text{In}_x\text{Ga}_{1-x}\text{N}$ and $\text{Al}_x\text{Ga}_{1-x}\text{N}$ ternary alloys measured by Osamura et al. [38] at room temperature (RT) is treated as

$$E_g(\text{In}_x\text{Ga}_{1-x}\text{N}) = x \cdot E_g(\text{InN}) + (1 - x) \cdot E_g(\text{GaN}) - \text{bowing} \cdot x \cdot (1 - x)$$

$$E_g(\text{Al}_x\text{Ga}_{1-x}\text{N}) = x \cdot E_g(\text{AlN}) + (1 - x) \cdot E_g(\text{GaN}) - \text{bowing} \cdot x \cdot (1 - x)$$

$$E_g(\text{Al}_x\text{In}_{1-x}\text{N}) = x \cdot E_g(\text{AlN}) + (1 - x) \cdot E_g(\text{InN}) - \text{bowing} \cdot x \cdot (1 - x)$$

and the bandgap energy of $\text{Al}_x\text{In}_y\text{Ga}_z\text{N}$ quaternary alloy is [39]

$$E_g(\text{Al}_x\text{In}_y\text{Ga}_z\text{N}) = \frac{xy T_{12} \left(\frac{1-x+y}{2} \right) + yz T_{23} \left(\frac{1-y+z}{2} \right) + xz T_{13} \left(\frac{1-x+z}{2} \right)}{x \cdot y + y \cdot z + z \cdot x}$$

$$z = 1 - x - y, \quad T_{ij}(u) = u \cdot E_{g,j} + (1 - u) \cdot E_{g,i} + \text{bowing}_{ij} \cdot u \cdot (1 - u)$$

Where “bowing” is the so-called bowing parameter (also called bowing vector), which is 7.0 eV for AlInN, 3.0 eV for InGaN, and 1.0 eV for AlGaN in our calculation, and the suffix 1, 2, and 3 is taken for AlN, InN, and GaN, respectively.

Table 3.2 Bandgap energy of GaN, AlN and InN related-temperature parameters

| Parameter | unit | GaN | AlN | InN |
|-------------------|-------|-------|-------|-------|
| $E_g(0\text{ K})$ | eV | 3.507 | 6.23 | 0.735 |
| α | meV/K | 0.909 | 1.799 | 0.245 |
| β | K | 830 | 1462 | 624 |

3.2.3 Band-offset ratio of III-nitride Alloys

The value of band-offset, which plays a very important role in the analysis of energy band diagram, is quite significant for the design of heterostructure devices. In some other textbooks, band-offset is also called band discontinuity, and it is obvious that when two different materials are grown next to each other, the conduction and the valence bands of the two materials will become discontinuous at the interface. However, the deviation of the determination of the band-offset values in semiconductor hetero-junction from experimental measurements and theoretical calculations exists large discrepancy which may be related to different factors in the following.

(A) Technical difficulty and often indirect nature of measurements,

(B) Possible dependence of band discontinuity on detailed, conditions of interface preparation,

(C) Strain dependence of band discontinuity.

And they may be related to the difficulty of obtaining high quality epitaxial films.

The conduction band offset ratio ($\Delta E_c / \Delta E_g$) for the AlN/GaN interface is between 0.66 and 0.81 according to the recent calculations [40]. In our study, a band offset ratio of 67/33 for the all interface is assumed principally.

3.2.4 Carrier transportaion of III-nitride Alloys

The physical model of carrier transport is the traditional drift-diffusion model for semiconductors. The specific equations can be expressed as

$$\vec{J}_n = q\mu_n n \vec{F} + qD_n \nabla n \quad (\text{for electrons})$$

and
$$\vec{J}_p = q\mu_p p \vec{F} + qD_p \nabla p \quad (\text{for holes})$$

where n and p are the electron and hole concentrations, \vec{J}_n and \vec{J}_p are the current densities of electrons and holes, \vec{F} is the electrostatic field, μ_n and μ_p are the mobilities of electrons and holes. The diffusion constants D_n and D_p are replaced by mobilities using the Einstein relation $D = \mu k_B T / q$. The equations used to describe the semiconductor device behavior are Poisson's equation,

$$\nabla \cdot (\epsilon_0 \epsilon \vec{F}) = q(p - n + p_D - n_A \pm N_f)$$

and the current continuity equations for electrons and holes,

$$\frac{1}{q} \nabla \cdot \vec{J}_n - R_n + G_n = \frac{\partial n}{\partial t} \quad (\text{for electrons})$$

$$\frac{1}{q} \nabla \cdot \vec{J}_p - R_p + G_p = \frac{\partial p}{\partial t} \quad (\text{for holes})$$

where ϵ is the relative permittivity. G_n and R_n are the generation rates and recombination rates for electrons, G_p and R_p are the generation rates and recombination rates for holes, respectively. The electric field is affected by the charge distribution, including the electron and hole concentrations, dopant ions p_D and n_A , and other fixed charges N_f that are of special importance in nitride-based devices due to the effect of built-in polarization.

Built-in polarization induced due to spontaneous and piezoelectric polarization is known to influence the performance of nitride devices. In order to consider the built-in polarization within the interfaces of nitride devices, the method developed by Fiorentini et al. is employed to estimate the built-in polarization, which is represented by fixed interface charges at each hetero interface. They provided explicit rules to calculate the nonlinear polarization for nitride alloys of arbitrary composition. [41]

Although the interface charges can be obtained by this theoretical model, experimental investigations often find weaker built-in polarization than that predicted by theoretical calculation. It is mainly attributed to partial compensation of the built-in polarization by defect and interface charges. [42] Typical reported experimental values are of 20%, 50% or

80% smaller than the theoretically calculated values. [43] As a result, 50% of the theoretical polarization values are used in our simulation from the average of the reported values.

A widely used empirical expression for modeling the mobility of electrons and holes is the Caughey Thomas approximation, which is employed in our calculation and can be expressed as [44]

$$\mu(N) = \mu_{\min} + \frac{\mu_{\max} - \mu_{\min}}{1 + (N/N_{\text{ref}})^\alpha}$$

where μ_{\max} , μ_{\min} , N_{ref} and α are fitting parameters. The parameter μ_{\max} represents the mobility of undoped or unintentionally doped samples, where lattice scattering is the main scattering mechanism, while μ_{\min} is the mobility in highly doped material, where impurity scattering is dominant. The parameter α is a measure of how quickly the mobility changes from μ_{\min} to μ_{\max} and N_{ref} is the carrier concentration at which the mobility is half way between μ_{\min} and μ_{\max} . The electron mobility of $\text{Ga}_{1-x-y}\text{Al}_x\text{In}_y\text{N}$ in our simulation can be expressed as

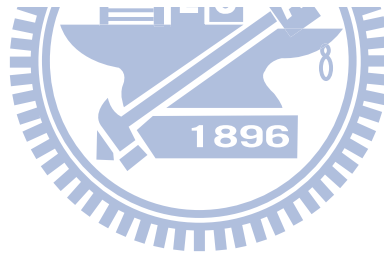
$$\mu_{\min}(\text{Ga}_{1-x-y}\text{Al}_x\text{In}_y\text{N}) = (1 - x - y) * \mu_{\min}(\text{GaN}) + x * \mu_{\min}(\text{AlN}) + y * \mu_{\min}(\text{InN})$$

$$\mu_{\max}(\text{Ga}_{1-x-y}\text{Al}_x\text{In}_y\text{N}) = (1 - x - y) * \mu_{\max}(\text{GaN}) + x * \mu_{\max}(\text{AlN}) + y * \mu_{\max}(\text{InN})$$

The relative parameters are summarized in Table 3.3.

Table 3.3 Mobility parameters of GaN, AlN and InN [29]

| Parameter (unit) | Electrons |
|--|---------------------|
| N_{ref} (cm^{-3}) | $1.0 \cdot 10^{17}$ |
| α | 1.37 |
| <i>GaN ; InN</i> | |
| μ_{max} ($\text{cm}^2\text{V}^{-1}\text{s}^{-1}$) | 684 |
| μ_{min} ($\text{cm}^2\text{V}^{-1}\text{s}^{-1}$) | 386 |
| <i>AlN</i> | |
| μ_{max} ($\text{cm}^2\text{V}^{-1}\text{s}^{-1}$) | 306 |
| μ_{min} ($\text{cm}^2\text{V}^{-1}\text{s}^{-1}$) | 132 |



Chapter 4 Study of Graded-composition electron blocking layer

4.1 Introduction

As the conception of inserting EBL mentioned before (Section 2.4), to reduce the carrier overflow in active region, an $\text{Al}_x\text{Ga}_{1-x}\text{N}$ EBL was usually used in common InGaN-based LED structures. However, For the band structure of the LED with EBL, as illustration of Fig. 4.1(a), the raised barrier height of the conduction band (CB) can hold electrons back. In the same way, the EBL moreover acts on holes. As well as the condition of CB, the larger band gap also brings the higher barrier height to the valence band (VB) and results holes inject more difficultly. Further, due to the spontaneous and piezoelectric polarization at the heterojunction interfaces for c-plane LEDs, the severe band bending leads the blocking layer to be a sloped triangular barrier and results in the higher potential barrier for holes, besides electrons. Furthermore, under a high driving current, the forward bias could make the n-side CB energy level higher than p-side, and the active region confinement of the EBL would be affected unsuccessfully.

In this chapter, the concept of band-engineering started from the observation on the band diagram of InGaN/GaN LEDs. If the composition of aluminum in EBL increases from the n-GaN side toward the p-GaN side, the band-gap broadens gradually. As a result, the barrier in the VB could be level down and even overturn, while the slope of the CB could be enhanced, as illustration of Fig. 4.1(b). Then, the improvement in capability of hole

transportation across the EBL as well as the electron confinement could be expected. To overcome the problem of the conventional EBL, we designed a linearly graded-composition of the $p\text{-Al}_x\text{Ga}_{1-x}\text{N}$ to replace the constant composition structure. For the gradual change of the band gap, it is expected to flatten the slope of VB edge and make the slope of CB edge cliffy simultaneously. As increasing the holes injection and preventing the electrons escape, the region of MQWs will collect more carriers and obtain more luminous intensity.

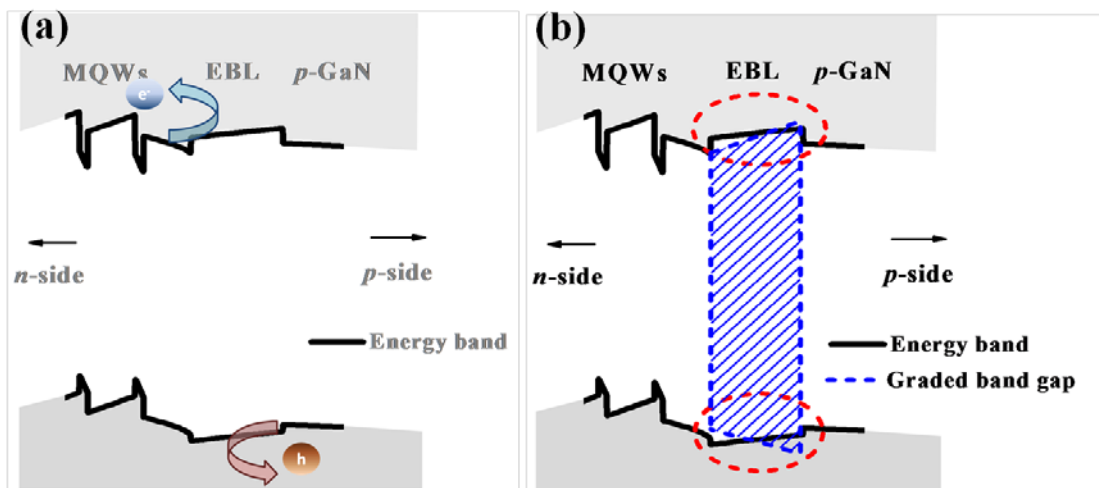


Fig.4.1 (a) The influence of inserting EBL between MQWs and p-GaN.
 (b) Schematic diagram of the concept of band engineering at EBL.

4.2 Simulation structure and parameter setting

To prove the feasibility of the hypothesis above, the band diagrams and carrier distributions in LED with GEBL were investigated first by APSYS simulation program. The simulation LED structures were composed of 4- μ m-thick n-type GaN layer (n-doping= $2 \times 10^{18} \text{ cm}^{-3}$), six pairs of $\text{In}_{0.15}\text{Ga}_{0.85}\text{N}/\text{GaN}$ multiple-quantum wells (MQWs) with 2.5-nm-thick wells and 10-nm-thick barriers, 20-nm-thick $\text{p-Al}_x\text{Ga}_{1-x}\text{N}$ EBL or GEBL (p-doping= $5 \times 10^{17} \text{ cm}^{-3}$), and 200-nm-thick p-type GaN layer (p-doping= $1 \times 10^{18} \text{ cm}^{-3}$) For the LEDs with GEBL, three types of GEBLs with compositions of aluminum graded along the (0 0 1) direction from 0% to 15%, 25%, and 35%, respectively, were simulated and denoted as LEDs A, B, and C. Furthermore for the conventional LED, the composition of aluminum was a constant of 15%.

Then, we put commonly accepted physical parameters to perform the simulations. The percentage of screening effect is 50% , the conduction-valence band offset ratio is 67:33 at all interfaces, the Shockley-Read-Hall recombination lifetime is 1ns, the Auger recombination coefficient in QWs is $2 \times 10^{-30} \text{ cm}^6/\text{s}$, and the internal loss is 2000m^{-1} , respectively.

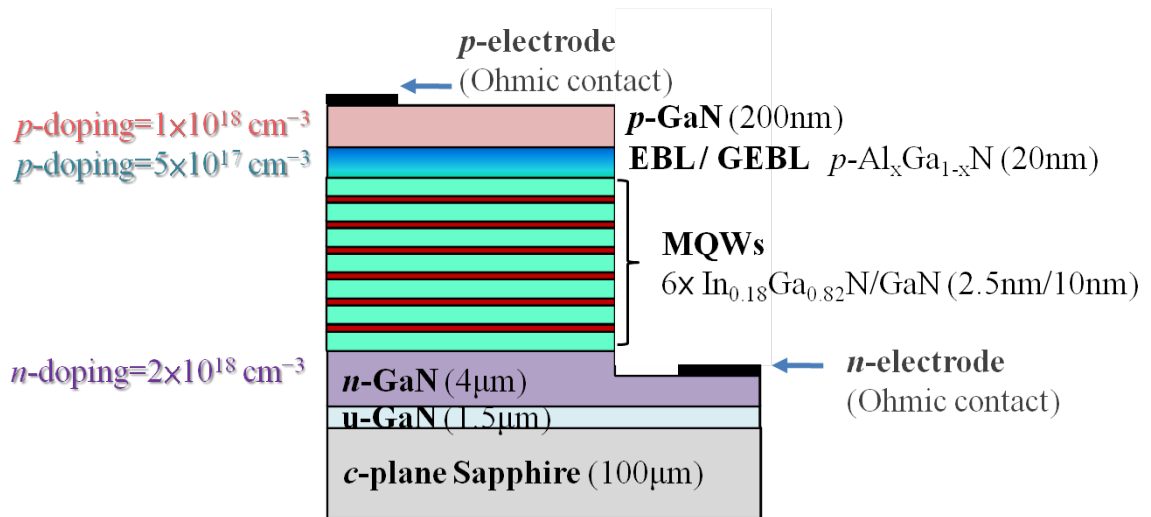


Fig. 4.2.1 The simulation structure of GEBL LEDs with material, thickness, and doping concentration.

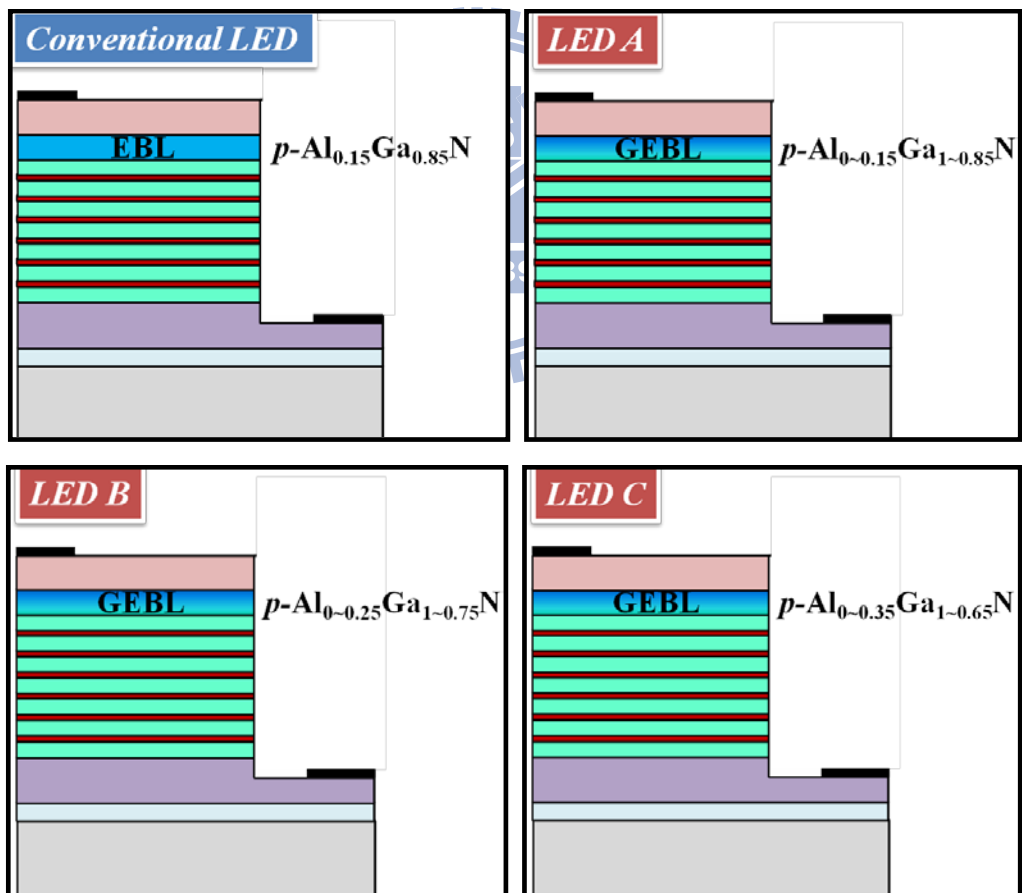


Fig. 4.2.2 The simulation structure of conventional LED, LED A, LED B, and LED C.

4.3 Calculated band diagrams and carrier distribution analysis

The calculated energy band diagrams of LEDs A, B, and C at current density of 100 A/cm² is illustrated in Figure 4.3.1. According to our concept of band-engineering, the degree of gradation had the decisive influence on the capability of holes injection.

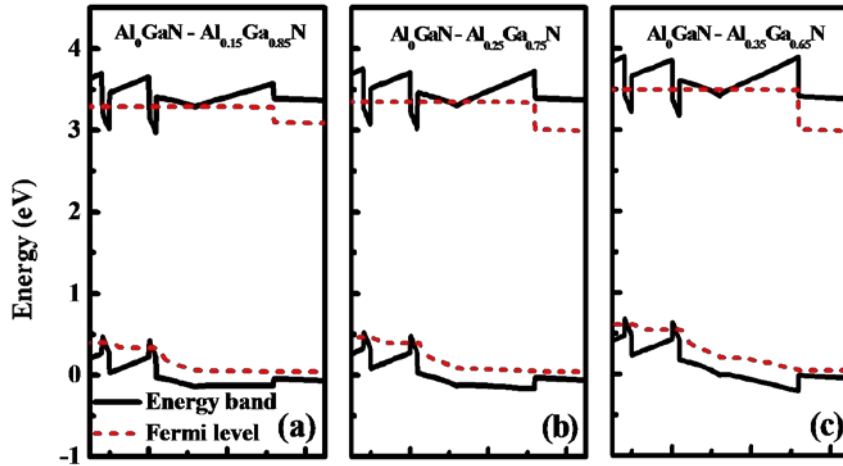


Fig. 4.3.1 Calculated energy band diagrams of (a) Al₀GaN to Al_{0.15}Ga_{0.85}N, (b) Al₀GaN to Al_{0.25}Ga_{0.75}N, and (c) Al₀GaN to Al_{0.35}Ga_{0.65}N graded-composition EBLs at a current density of 100 A/cm².

Even with small degree of gradation as LED A, the slope of the VB can be leveled. Then the slope starts to overturn when the composition of aluminum at the p-side increases up to 25%. Moreover, it is worth noting that the valence band offset (ΔE_v) between the last GaN barrier and the EBL is diminished in all three LEDs with GEBL. Therefore, the hole injection can be improved effectively by using the GEBL. In the meantime, as the degree of gradation increased, the conduction band offset at the interface of p-GaN and EBL increases as well, so does the confinement capability of electrons. But correspondingly, the ΔE_v between EBL and

p-GaN increases as the composition of aluminum rises, which might retard the transportation of holes.

Then, for further analysis of band changes under different current injection, we list the band diagrams at EBL region (20, 100, and 300 A/cm²) in Figure 4.3.2.

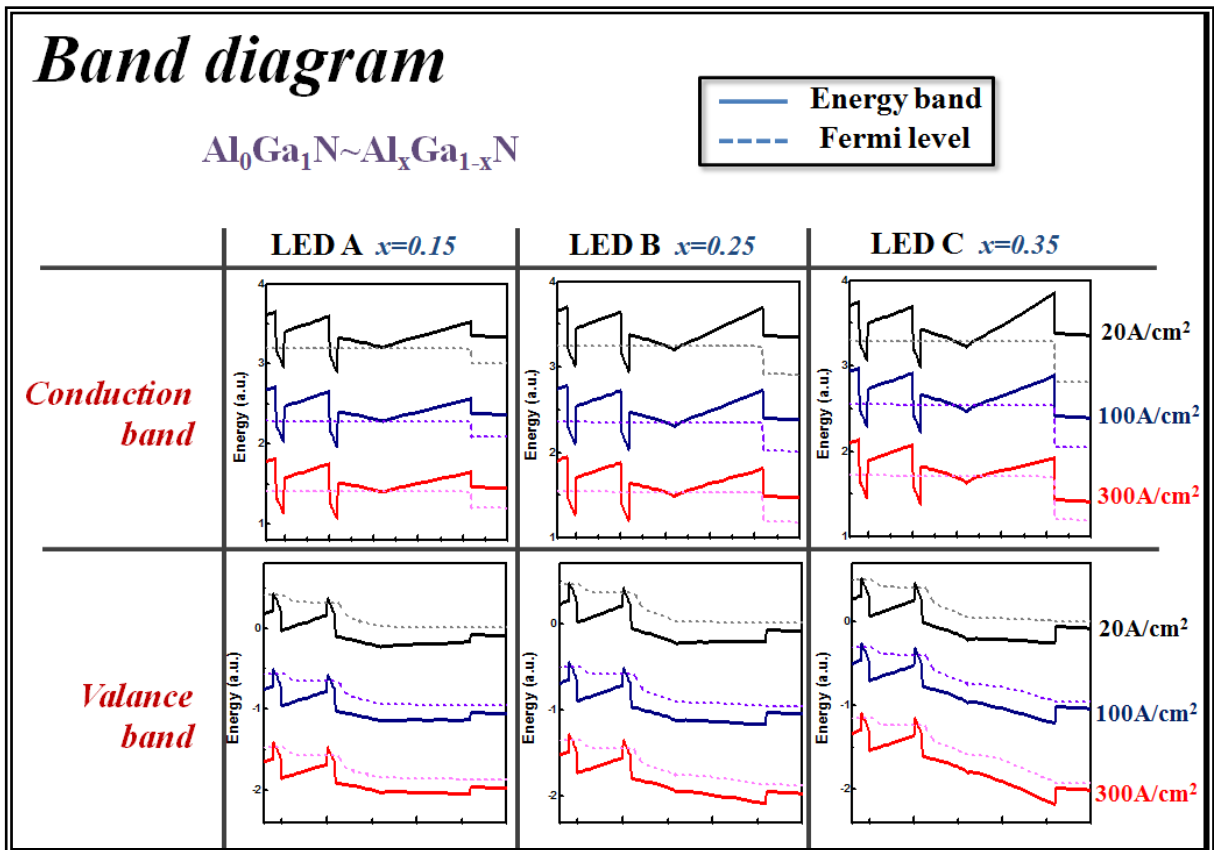
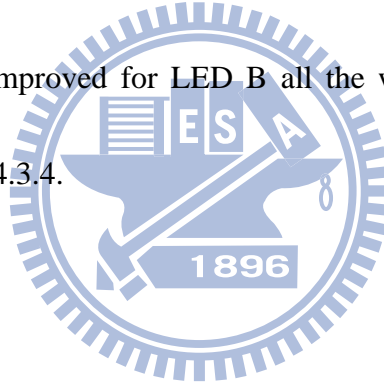


Fig. 4.3.2 The calculated band diagram of GEBL LEDs at 20, 100, and 300 A/cm²

For conduction bands, although all GEBL LEDs show upward band edge in EBL region, the slopes of EBL band edge are flatter as current increasing. The lessened effective barrier height causes the electron overflow severer under high injection, as shown in Fig. 4.3.3. From this illustration of electron leakage, it can be seen that the electron overflow of conventional

LED always exist at 20 A/cm^2 to 300 A/cm^2 . On the contrary, for all GEBL LEDs, this overflow phenomenon can be suppressed drastically at 20 A/cm^2 . However, as injection current rising to 300 A/cm^2 , electron leakage of LED A and LED C come alive. The leakage reason of LED A is its smaller barrier height limits. On the other hand, for LED C with the largest grading composition of aluminum (0~30%), the energy band of EBL is bent down under high forward bias (high current injection, 300 A/cm^2) and lead to electron overflow. Therefore, from current injection of 20 A/cm^2 to 300 A/cm^2 , only LED B stands out above the GEBL LEDs and suppress electron overflow successfully. Of course the most important reason is that holes injection are improved for LED B all the while, under high injection current especially, as shown in Fig. 4.3.4.



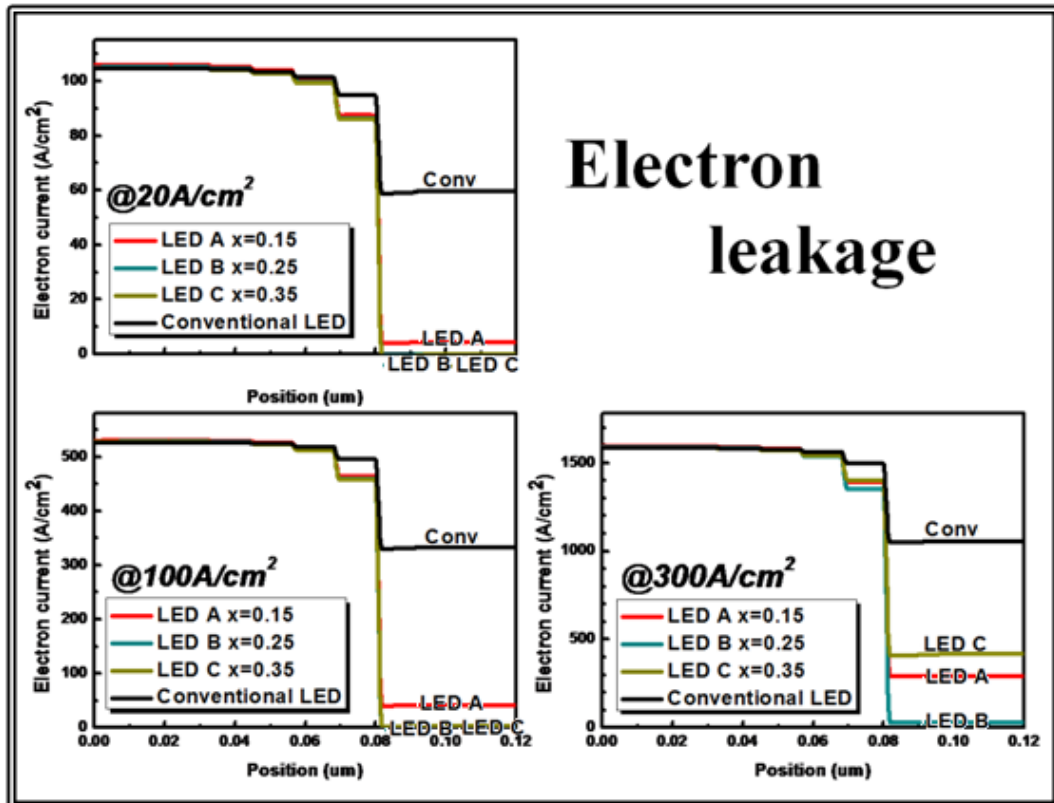


Fig. 4.3.3 Simulated electron current density for conventional LEDs and GEBL LEDs

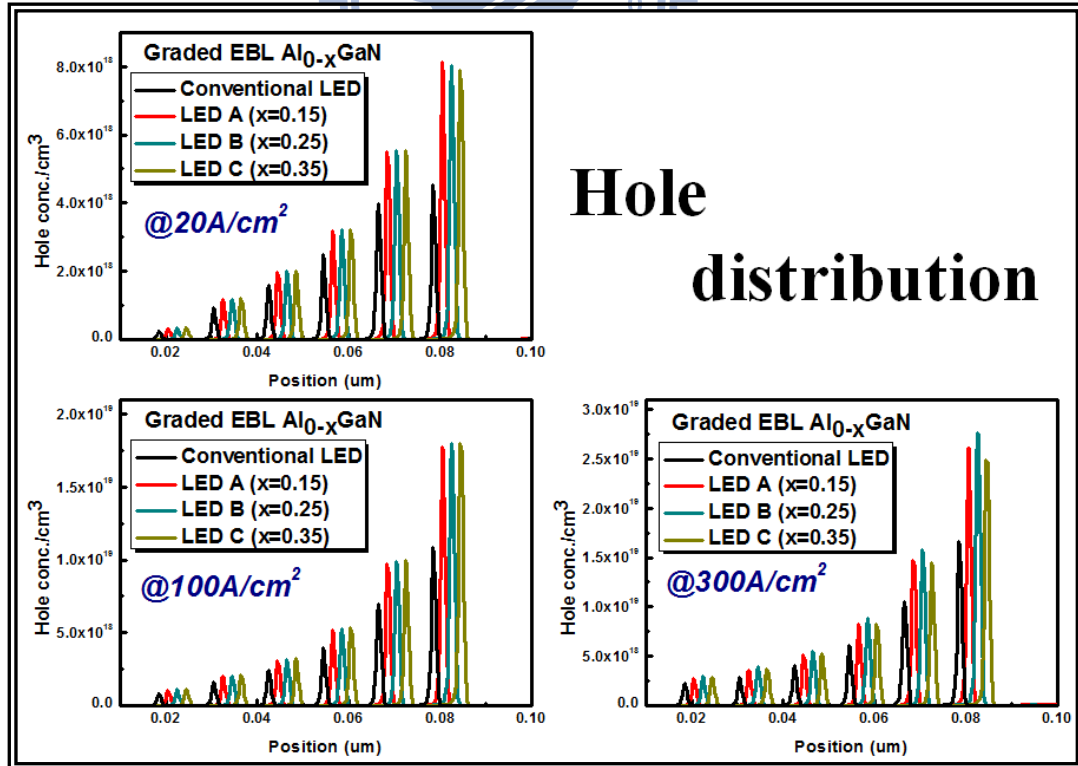


Fig. 4.3.4 Distribution of hole concentration of conventional LEDs and GEBL LEDs

In addition, high aluminum composition EBL is not practical for actual application due to the low acceptor-activation efficiency and the low crystal quality in epitaxy. Consequently, only LED B with aluminum graded from 0% to 25% is discussed in detail in the following paragraph.

The profiles of hole and electron concentration distribution at a current density of 100 A/cm² are illustrated in Figs. 4.3.5(a) and 4.3.5(b), respectively. It can clearly be seen that with GEBL, injected holes uniformly distribute along the EBL region compared to conventional one, demonstrating that the flat valence band indeed favored the hole transportation across EBL. Meanwhile, the hole concentration in MQWs is significantly increased as expected. Moreover, the electron concentration in MQWs is also enhanced, while the electron distribution within the GEBL region and p-GaN is enormously decreased over two orders. This result indicates that GEBL can suppress the electron overflow out of active region more effectively than conventional EBL, even though the conduction band offset between the last GaN barrier and the GEBL is diminished.

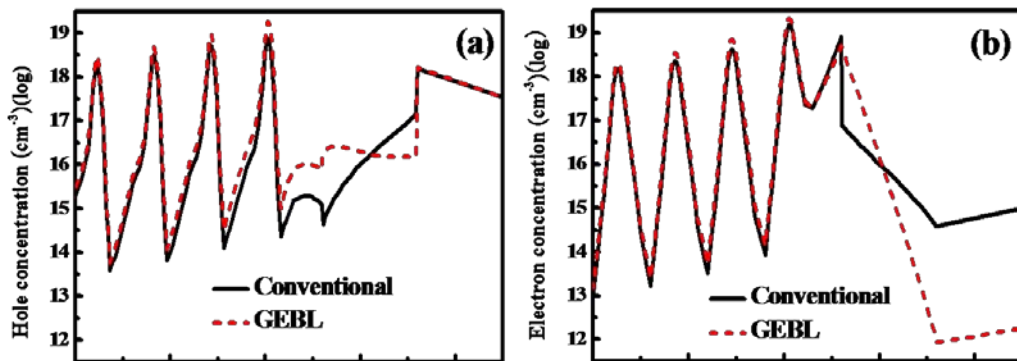


Fig. 4.3.5 Calculated (a)hole concentration distribution and (b)electron concentration distribution of conventional and GEBL LEDs at a current density of 100 A/cm².

4.4 Sample structure and Fabrication

The LED structures with EBL and GEBL were grown on c-plane sapphire substrates by MOCVD. After depositing a low temperature GaN nucleation layer, a 4 μm n-type GaN layer, and a ten-pair InGaN/GaN superlattice prestrain layer, the rest of the LED structures were grown based on our simulation design. The epitaxial recipe for the GEBL is worth noting. Generally, the graded-composition ternary III-nitride semiconductors can be grown by two methods: growth temperature ramping and III/III ratio ramping. [45, 46] Here we adopted the Al/Ga ratio ramping because the temperature ramping would change the growth rate, and the higher temperature might damage the quality of QWs. The growth temperature of conventional EBL and GEBL was the same (870 $^{\circ}\text{C}$), and the aluminum composition profile of the GEBL was approximately graded from 0% to 25%. Finally, the LED chips were fabricated by regular chip process with ITO current spreading layer and Ni/Au contact metal, and the size of mesa is 300 \times 300 μm^2 . The sample structure is shown in Fig. 4.4.1. The fabrication processes of sample LED are shown in Fig. 4.4.2.

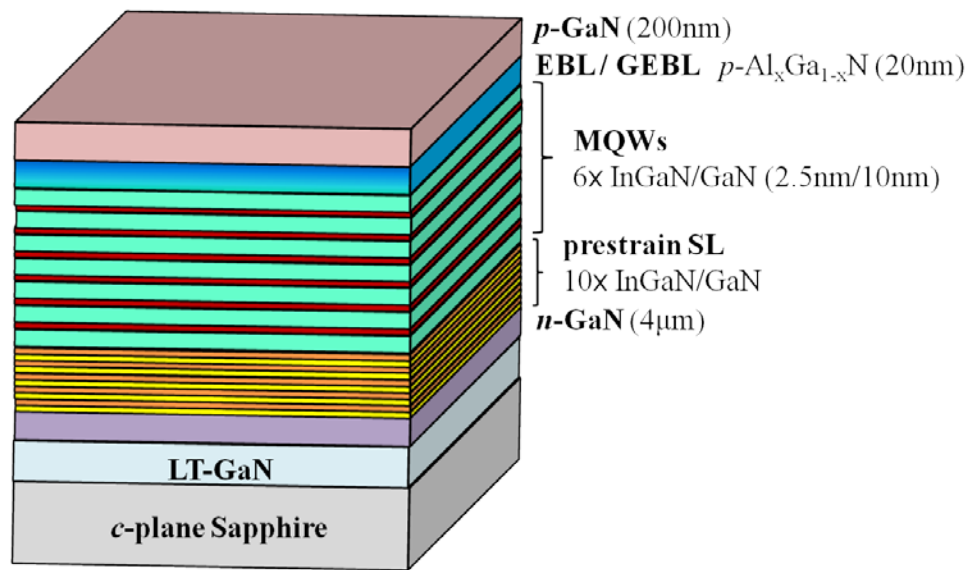


Fig.4.4.1 The schematic drawing of sample structure (GEBL LED).

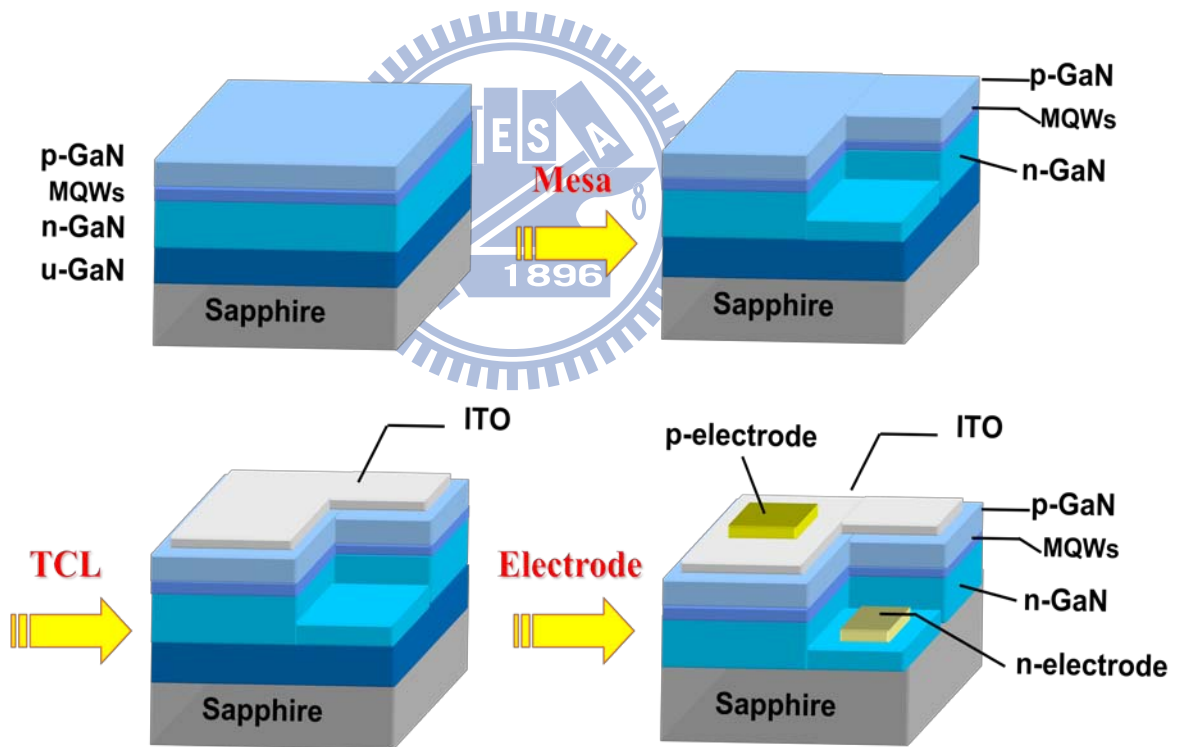


Fig.4.4.2 The schematic drawing of fabrication processes of LED.

4.5 Analysis of carrier-dependence EL efficiency and efficiency droop behavior

Fig. 4.5.1 shows the L - I - V curves of the conventional and GEBL LED. The output powers were measured with a calibrated integrating sphere. The forward voltages (V_f) at 22 A/cm^2 and series resistances (R_s) of GEBL LED are 3.28 V and 7 Ω , respectively, which are lower than that of 3.4 V and 8 Ω for conventional LED. The reduced V_f and R_s can be attributed to the improvement in hole injection and the higher-efficiency p-type doping in GEBL. [47] In the case of L - I curves in Fig. 4.5.1, although the output power of GEBL LED is a little lower at low current density (below 30 A/cm^2), it increases more rapidly as the injection current increases as compared to the conventional one. The output powers were enhanced by 40% and 69% at 100 and 200 A/cm^2 , respectively. This phenomenon can be explained as follows: at low current density, it is more difficult for holes to tunnel across the barrier at the interface of p-GaN and EBL in GEBL LED because the ΔE_v is larger than that in conventional LED. While at high current density, the tunneling process of holes can be negligible, and the diffusion process is dominated for the hole transportation into the MQW.[32] As discussed above, the diffusion process in GEBL is much easier than that in conventional one due to the flat valence band and much lower ΔE_v at the interface of the last GaN barrier and EBL. In conjunction with the superior electron confinement, much stronger light output was achieved in GEBL LED at high current density.

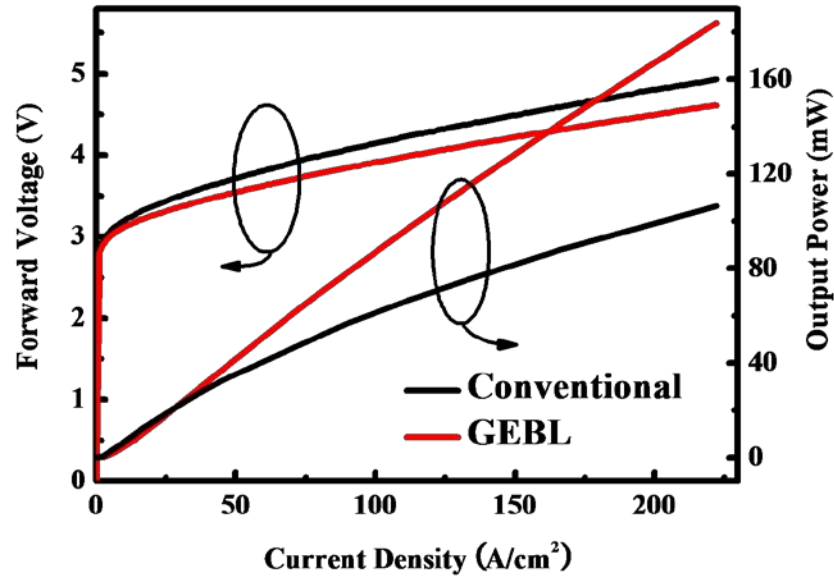


Fig. 4.5.1 Forward voltage and output power as a function of current density for conventional and GEBL LEDs.

Finally, the normalized efficiency of conventional and GEBL LEDs as a function of current density was investigated, as shown in Fig. 4.5.2. The maximum efficiency (η_{peak}) of GEBL LED appears at an injection current density of 80 A/cm², which was much higher than that for conventional LED (at 20 A/cm²). More interestingly, the efficiency droop, defined as $(\eta_{\text{peak}} - \eta_{200 \text{ A cm}^{-2}}) / \eta_{\text{peak}}$, was reduced from 34% in conventional LED to only 4% in GEBL LED. This significant improvement in efficiency can be mainly attributed to the enhancement of hole injection as well as electron confinement, especially at high current density.

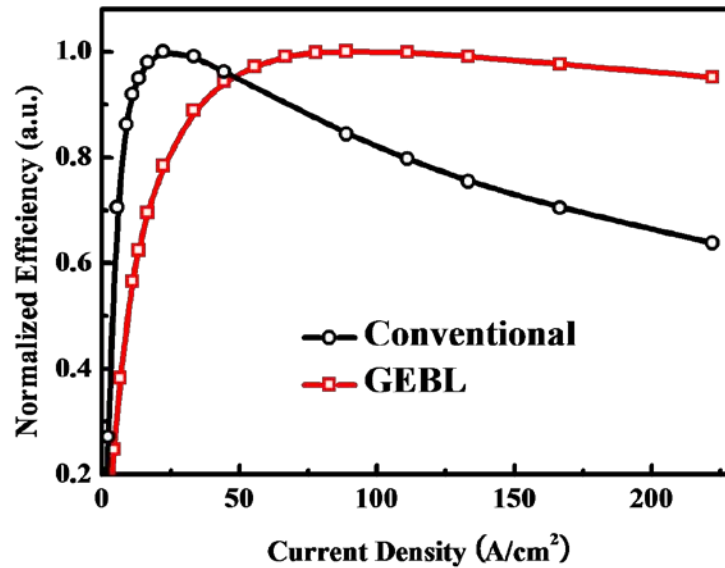
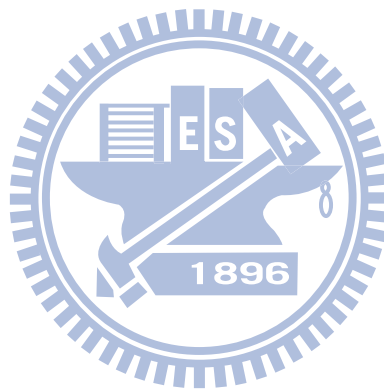


Fig. 4.5.2 Normalized efficiency as a function of current density for conventional and GEBL LEDs

4.6 Summary

In conclusion, we have designed a graded-composition electron blocking layer for InGaN/GaN LED by employing the band-engineering. The simulation results showed that the triangular barrier of conventional EBL at the valence band could be balanced, while the slope of the conduction band could be increased by increasing the band-gap of $\text{Al}_x\text{Ga}_{1-x}\text{N}$ along the (0001) direction. As a result, the hole concentration in MQWs was significantly increased, while the electron distribution within the GEBL region and p-GaN was enormously decreased over two orders, indicating that the GEBL can effectively improve the capability of hole transportation across the EBL as well as the electron confinement. Furthermore, the LED structure with GEBL was realized by MOCVD. The L-I-V characteristics of GEBL LED showed the smaller V_f and R_s due to the improvement in hole injection and the

higher-efficiency p-type doping in GEBL as compared to the conventional LED. More importantly, the efficiency droop was reduced from 34% in conventional LED to only 4% in GEBL LED. This work implies that carrier transportation behavior could be appropriately modified by employing the concept of band-engineering.



Chapter 5 Study of InGaN-Based UV LED with InAlGaN Barrier

5.1 Introduction

GaN-based ultraviolet (UV) LEDs have attracted great attention in last few years due to its potential applications in photo-catalytic deodorizing such as air conditioner,[48] and there have been interests in solid-state lighting by using near-UV LEDs light for the phosphor-converting source.[49, 50] However, it is difficult to fabricate near-UV LEDs with high efficiency, because the external quantum efficiency (EQE) decreases drastically below the wavelength of 400 nm.[51] This is due to the smaller InN mole fluctuation with reduced indium composition in the near-UV quantum wells (QWs), and thus less localized energy states lead to lower efficiency of the near-UV LEDs.[52, 53] Moreover, crystalline quality and light absorption of GaN are significant for short wavelength near-UV LEDs.[54, 55] It's well known that in low indium content InGaN QWs, AlGaN barrier is necessary for carrier confinement. But the two materials of AlGaN and InGaN are very different in growth temperature which affects strongly on the quality of material and device performances. To improve the quantum efficiency of the InGaN-based LEDs, previous reports use of InAlGaN in the quantum barrier instead of AlGaN or GaN for polarization, strain, material quality and interfacial abruptness (band offset) issues.[21, 56-61]

It was also found that by introducing of indium in low temperature (LT) AlGaN layer to be effective in improving the PL intensity, smooth morphology, interfacial abruptness and

crystalline quality.[62] However, by introducing of indium in AlGaInN without increase aluminum content will cause the injustice of the quantum confined Stark effect (QCSE) and bandgap issues.

Previous studies have indicated that electron leakage from the active region is enhanced by strain-induced polarization charges at heterointerfaces that result from polarization mismatch between layers in a conventional LED active region.[31] Therefore, in 2008, [21]Schubert's team switched materials for the active region from the conventional GaN barrier to polarization matching InAlGaInN to eliminate the charges and cuts droop, raising power output by 25 % at high currents.

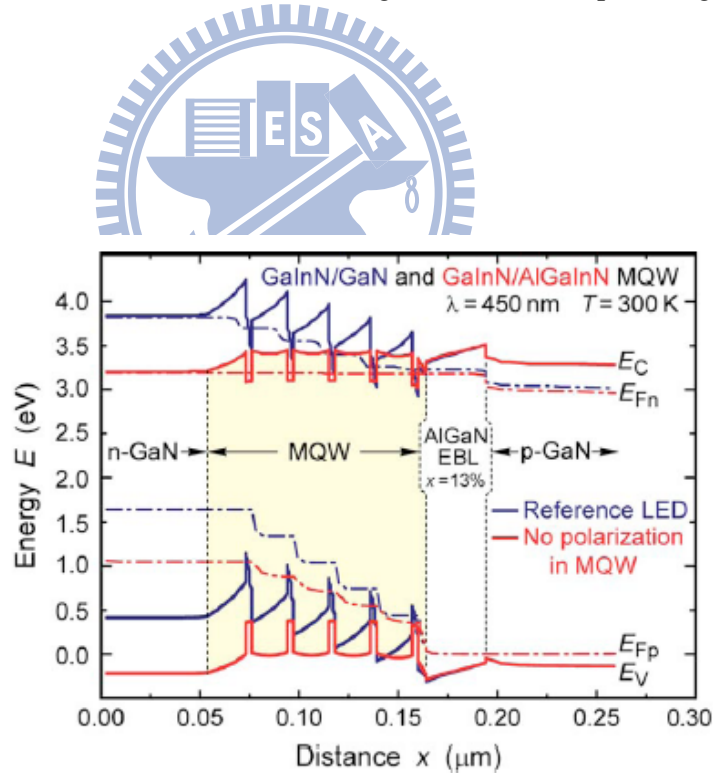


Fig. 5.1.1 Calculated band diagram of reference GaInN/GaN LED as well as AlGaInN LED structure with polarization-matched MQW under a forward bias condition. [31]

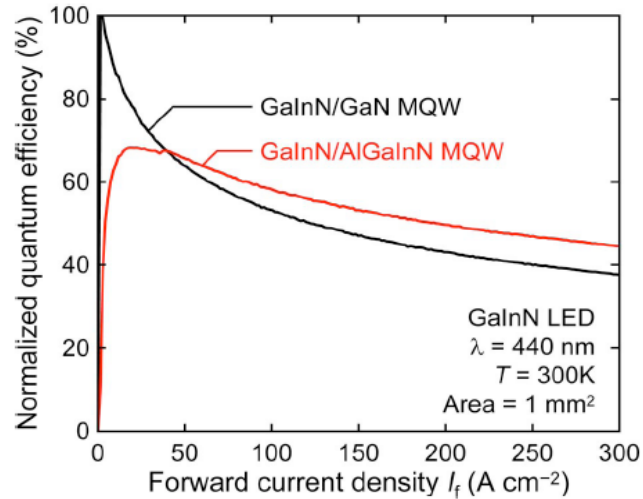


Fig. 5.1.2 Normalized EQE as a function of forward current density for GaInN/AlGaInN MQW LEDs and reference GaInN/GaN MQW LEDs. [21]

In this study, the InAlGaN barrier was not for polarization, lattice or bandgap matched in InGaN quantum well, but matched in optimized AlGaInN barrier for a fair investigation on the light output and efficiency current droop characteristics. We found other advantage with InAlGaN barrier and investigated by simulation in depth.

5.2 Sample structure and fabrication

All samples used in this study were grown on 2 inch c-plane sapphire substrates using a atmospheric-pressure metal organic chemical vapor deposition (AP-MOCVD SR4000) system. For the growth of GaN-based LEDs, trimethyl gallium (TMGa), trimethyl indium (TMIn), trimethyl aluminum (TMAI), and ammonia (NH₃) were used as the source precursors for Ga, In, Al, and N, respectively. Silane (SiH₄) and bis-cyclopentadienyl magnesium

(Cp_2Mg) were used as n-type and p-type dopants. The conventional structure of InGaN/AlGaN multiple quantum wells (MQWs) UV LEDs consists of a low-temperature (500°C) 30-nm-thick GaN nucleation layer, a $1\text{-}\mu\text{m}$ -thick un-doped GaN buffer layer, a $2.5\text{-}\mu\text{m}$ -thick Si-doped AlGaN cladding layer, an 10 periods of InGaN/AlGaN MQWs active region, a 15-nm-thick Mg-doped AlGaN first cladding layers, a 10-nm-thick Mg-doped AlGaN second cladding layers, and a 60-nm-thick Mg-doped GaN contact layer. The sample structure of InGaN/InAlGaN MQW was almost identical to that of the InGaN/AlGaN MQW LED, the only difference is that we used InAlGaN instead of AlGaN as the barrier layers in the active region. Here, the MQW active region consisted of ten periods of 2.6-nm-thick un-doped $\text{In}_{0.025}\text{Ga}_{0.975}\text{N}$ well layers and 11.7-nm-thick Si-doped $\text{In}_{0.0085}\text{Al}_{0.1112}\text{Ga}_{0.8803}\text{N}$ or $\text{Al}_{0.08}\text{Ga}_{0.92}\text{N}$ barrier layers growth on n- $\text{Al}_{0.02}\text{Ga}_{0.98}\text{N}$ / ud-GaN / Sapphire. The sample structure is shown in Fig. 5.2.

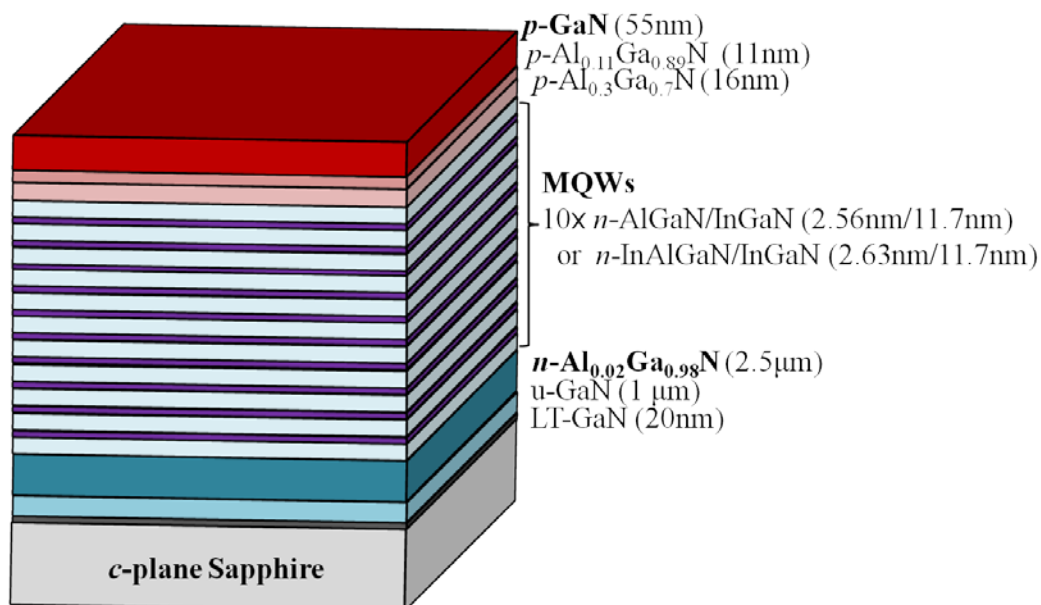


Fig. 5.2 The schematic drawing of sample structure (UV LED)

5.3 Investigation of optical property and surface morphology

For investigation of surface morphology, a 50-nm InAlGaN and AlGaN film layer were also deposited on n-AlGaN/ud-GaN/Sapphire substrate. High-resolution double crystal x-ray diffraction (DCXRD) was used to identify *Al* and *In* mole fractions of MQWs. These samples were also characterized by room temperature photoluminescence (PL), atomic force microscopy (AFM) and transmission electron microscopy (TEM) to reveal the optical property, surface morphology and MQWs structure, respectively.

PL spectra of AlGaN and InAlGaN film grown on n-AlGaN/ud-GaN/Sapphire substrate were obtained at a room temperature to investigate the band edge emission. Fig. 5.3.1 shows that the PL emission energy of these two samples are very close about 3.594 (eV) and the peak intensity of InAlGaN is slightly higher than AlGaN. The strong PL emission is attributed to the better crystal quality.[62] Insert in Fig. 5.3.1 shows the surface morphology of the two films AlGaN and InAlGaN with the same thickness about 50-nm. The root-mean-square (RMS) roughness measured by AFM is about 0.813 nm and 0.595 nm, respectively. The relatively high roughness of AlGaN film can mainly be attributed to the low deposition temperature of 830°C necessary for the adjacent InGaN well.

Fig. 5.3.2(a) shows the HRXRD (ω -2 θ) curves in the (002) reflections of InGaN/AlGaN and InGaN/InAlGaN MQWs. The results show that the locations of multiple satellite peaks of InGaN/AlGaN and InGaN/InAlGaN MQWs are very close. This indicates that the thickness

of barrier layer in these two samples is matched, and it is quite consistent with the measured values of 11.7 nm from HRTEM images as shown in Fig. 5.3.2(b) and Fig. 5.3.2(c). In addition to estimate the Indium and Aluminum composition in the MQWs, we simulate the HRXRD (ω - 2θ) curve by using dynamical diffraction theory. The In composition in the QWs was determined to be about 2.5%, where the thickness of the well was about 2.6 nm. The compositions of ternary and quaternary barriers were $\text{Al}_{0.08}\text{Ga}_{0.92}\text{N}$ and $\text{In}_{0.0085}\text{Al}_{0.1112}\text{Ga}_{0.8803}\text{N}$, respectively.

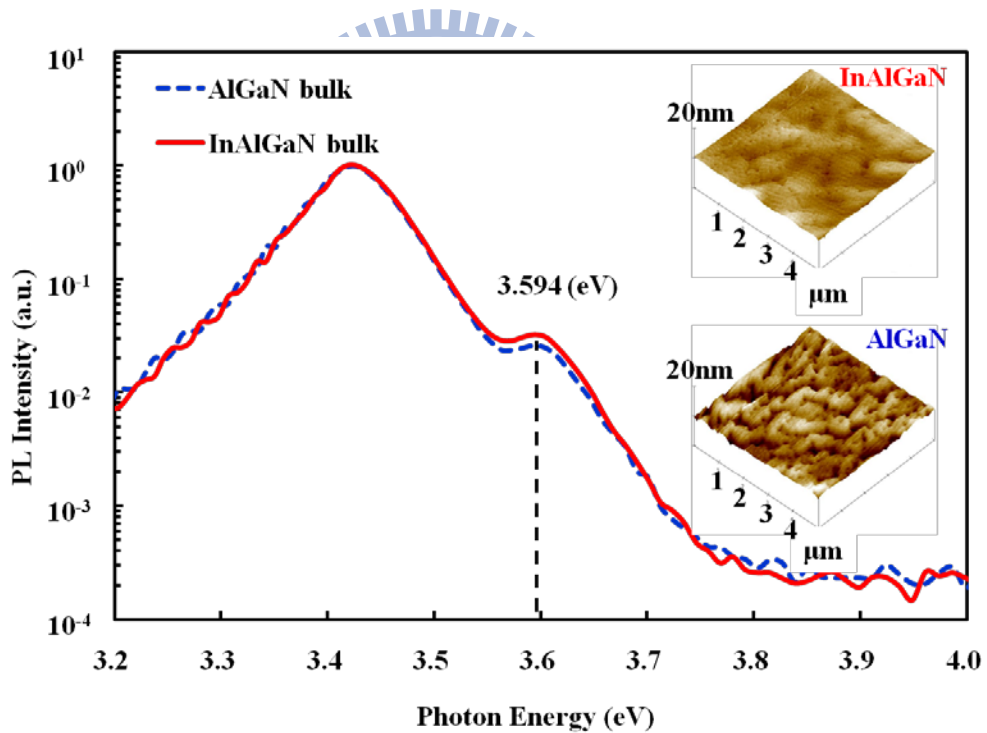


Fig 5.3.1 Room-temperature PL spectra of AlGaN and InAlGaN bulks. Insert Figs. shows surface morphology AFM over $5 \times 5 \mu\text{m}^2$ of bulk AlGaN (RMS:0.813 nm) and InAlGaN (RMS:0.595 nm) layer with thickness about 50 nm.

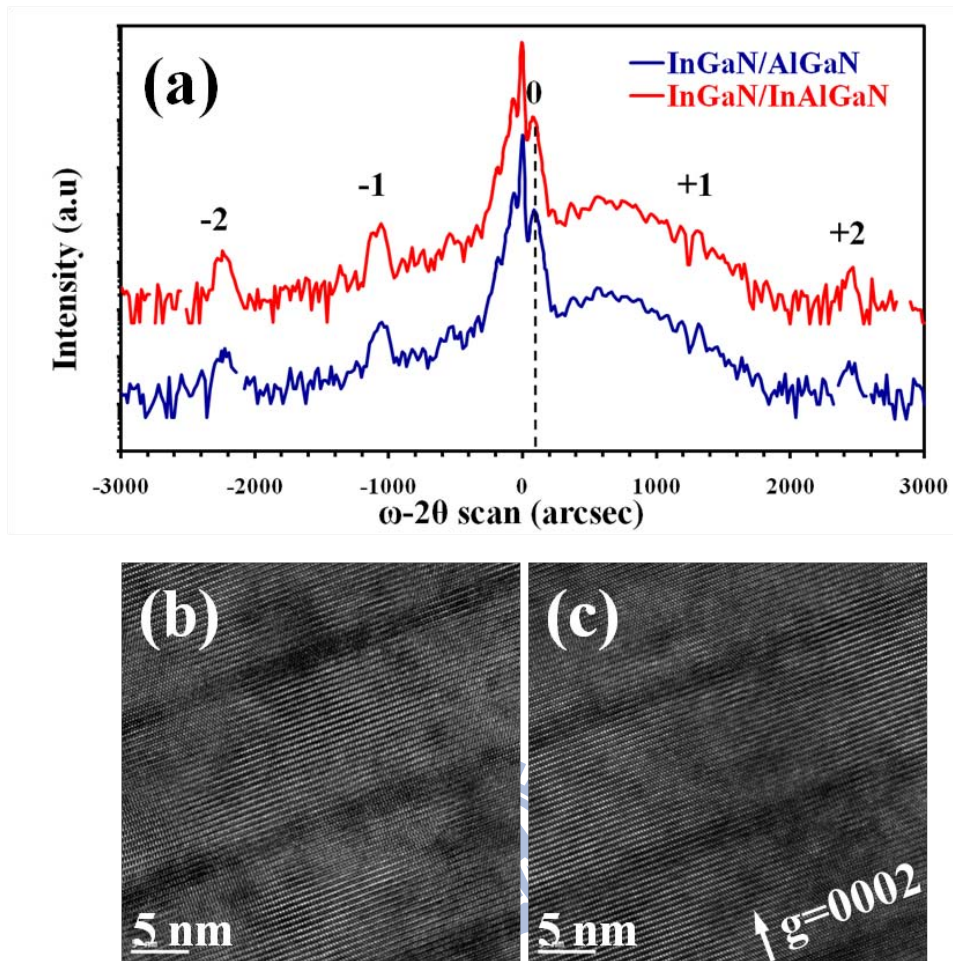


Fig. 5.3.2 (a)HRXRD (ω - 2θ) curves in the (002) reflections of InGaN/AlGaN and InGaN/InAlGaN MQW. Cross-sectional TEM images of (b) InGaN/AlGaN and (c) InGaN/InAlGaN MQW. The diffraction condition is $g=0002$.

5.4 Current-dependent intensity and efficiency

The electrical properties of UV LED with ternary and quaternary barrier are shown in Fig. 5.4. Fig. 5.4(a) shows the light output power–current–voltage (L-I-V) characteristics for the AlGaN and InAlGaN barrier UV LEDs. The forward voltage was 3.89 and 3.98 V for InGaN/AlGaN and InGaN/InAlGaN MQWs UV LED at a forward current of 350 mA, respectively. A little high forward voltage of InAlGaN barrier LED can be attributed to the

higher Al content compare to the AlGa_N barrier, thus enhance the series resistance in the device. The light output power of InGa_N-based UV LED with the InAlGa_N barrier is higher by 25% and 55% than the AlGa_N barrier at 350 mA and 1000 mA, respectively. Fig. 5.4(b) shows the normalized efficiency curves as a function of forward current for the two samples. For the InGa_N/AlGa_N UV LEDs, when the injection current exceeds 1000 mA, the efficiency is reduced to 66% of its maximum value. In contrast, InGa_N/InAlGa_N UV LEDs exhibit only 13% efficiency droop when increasing the injection current to 1000 mA. The reduction of efficiency droop is quite clear and the current at maximum efficiency shifts from 150 to 400 mA.



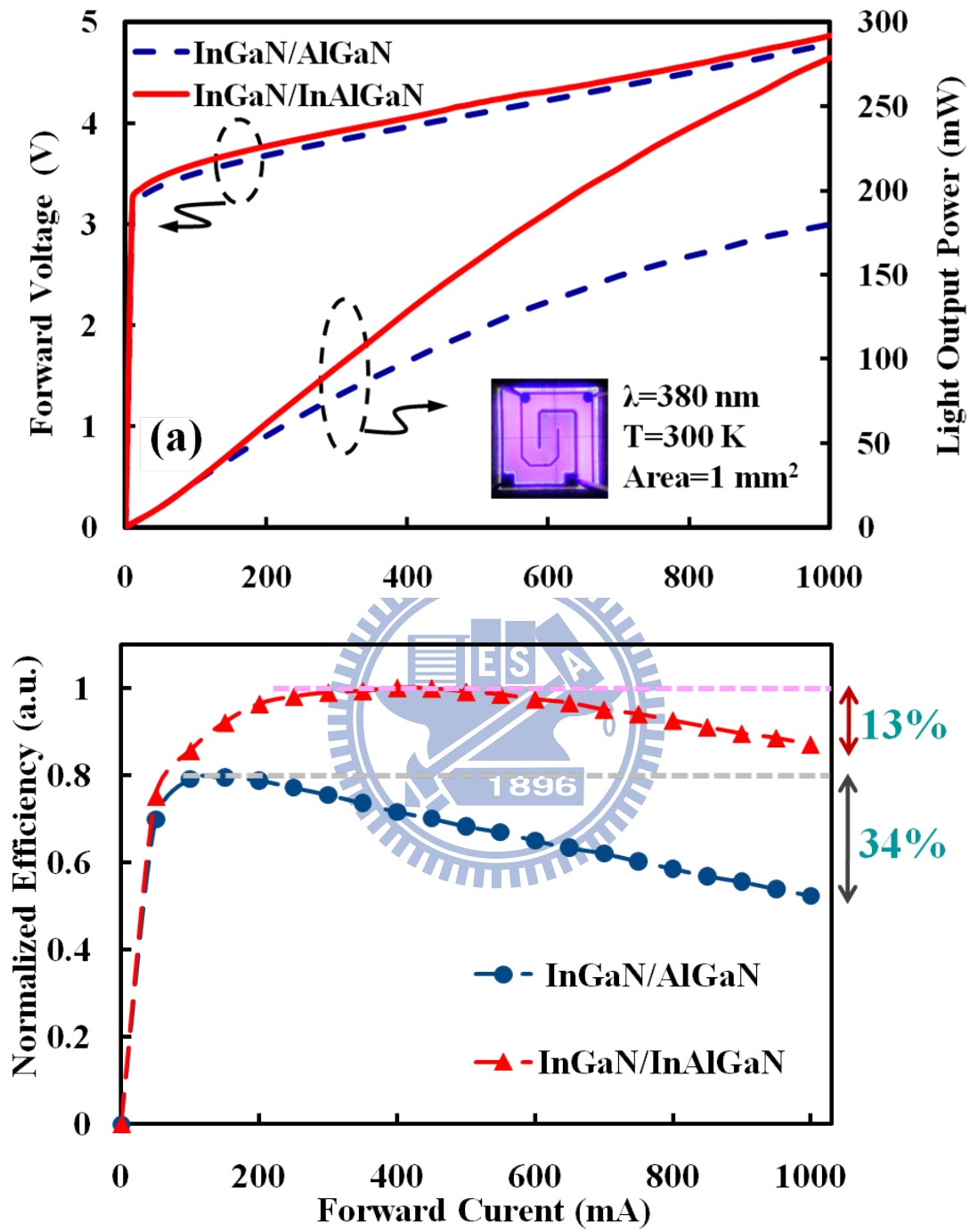


Fig. 5.4 (a) L-I-V curves of the LEDs with AlGaN (dash) and InAlGaN (solid) barrier. (b) Normalized Efficiency curves of experimental. Insert in Fig. 5.4(a) shows the mesa-type UV chips.

5.5 Theoretical analysis

In order to investigate the physical origin of efficiency droop in these UV LEDs, we investigated the above structures by using the APSYS simulation software. Commonly accepted Shockley-Read-Hall recombination lifetime (several nanoseconds) and Auger recombination coefficient (about $\sim 10^{-30} \text{ cm}^6 \text{ s}^{-1}$) are used in the simulations. In addition, because of lattice match in barrier between AlGa_{0.975}N and InAlGa_{0.92}N, we can exclude the effect of total polarization fields including spontaneous and piezoelectric polarizations. The total polarization fields can be obtained through the calculation of the In_{0.025}Ga_{0.975}N, Al_{0.08}Ga_{0.92}N and In_{0.0085}Al_{0.1112}Ga_{0.8803}N for the -0.0305, -0.0391 and -0.0398 (Cm^{-2}), respectively.[63] Therefore, we use the same factor of 50% for charge screening effect. However, the preliminary simulation results cannot fit in with experiment. Thus, it must have some reasons for this outstanding UV LED with InAlGa_{0.92}N barrier, and here we intend to consider carrier mobility and band offset ratio as factors on droop behavior for these UV LEDs.

5.5.1 Carrier mobility issue

It's difficult to calculate minority carrier hole mobility in semiconductor material because of the degenerate valence bands. On the other hand, as mentioned before in Sec 3.2.4, the majority carrier electron mobility of Ga_{1-x-y}Al_xIn_yN can be calculated by Caughey Thomas approximation. In our simulation, the calculated electron mobility is $354 \text{ cm}^2/\text{V}^{-1}\text{s}^{-1}$ for

$\text{Al}_{0.08}\text{Ga}_{0.92}\text{N}$ and $642 \text{ cm}^2/\text{V}^{-1}\text{s}^{-1}$ for $\text{In}_{0.0085}\text{Al}_{0.1112}\text{Ga}_{0.8803}\text{N}$, respectively. Hence, to investigate the efficiency droop in these two samples, we assume that InGaN-based UV LED with InAlGaN barrier has relatively high carrier mobility.

To prove above hypothesis, we vary the carrier mobility of InAlGaN depending on the value of AlGaN. These simulation results are shown in Fig 5.5.1. It can clearly be seen that the droop behavior is dominated by hole mobility, and we find the efficiency curve will nearest to the experimental result when hole mobility of InAlGaN is about 5 times the value of AlGaN. However, this value of hole mobility for InAlGaN compared with AlGaN is seemed unreasonable.

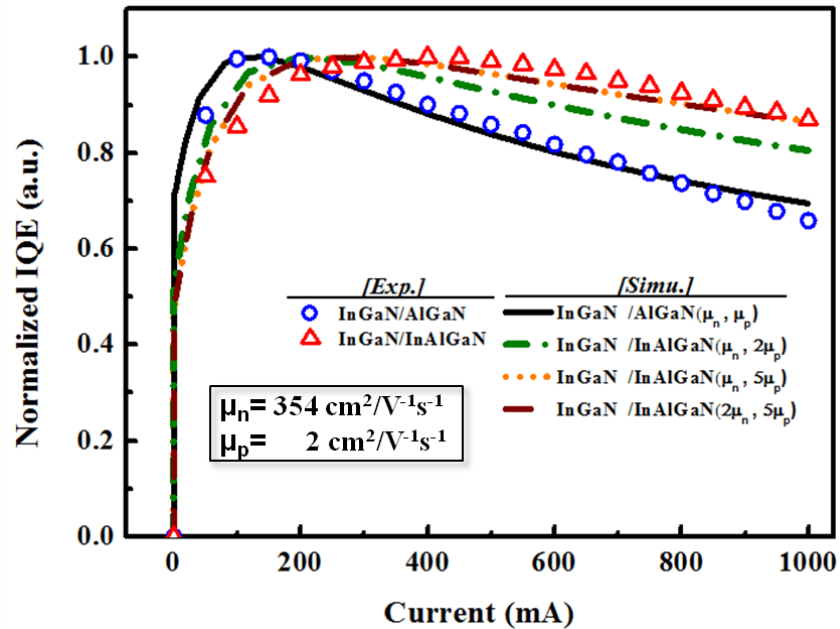


Fig. 5.5.1 Simulation results of normalized IQE under different carrier mobility.

5.5.2 Band offset ration issue

Besides, a different band-offset ratio is also considered in our simulation. Former researches indicated the band offset ratio is between 6:4 and 7:3 for InGaN/(Al)InGaN heterojunction. [64]

For UV LED with InAlGaN barrier, after simulating with band offset ratio from 5:5 to 7:3, both the efficiency droop behavior can be elevated with higher band offset ratio, as shown in Fig. 5.5.2. Therefore, the band offset ratio from 6:4 to 7:3 is used in this simulation for introducing of indium in AlGaN. We can know that under the same energy bandgap of barrier, the band-offset ratio from 6:4 to 7:3 will lead to higher conduction-band offset and lower valence-band offset between well and barrier. This is useful for electron confinement and hole distribution in low indium content InGaN-based UV LEDs.

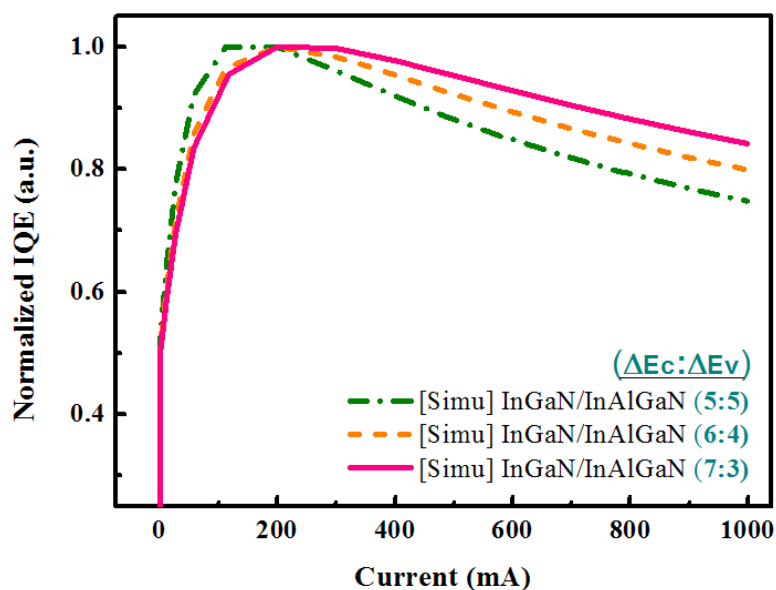


Fig. 5.5.2 Simulation results of normalized IQE under different band offset ratio.

5.5.3 Conclusion

Finally, we performed the numerical simulation with different parameters in band-offset ratio and carrier mobility, listed in Table 5.1. The results of the EQE droop simulation of both different structures are in good agreement with the experimental data as shown in Fig. 5.5.3.

Furthermore, we investigated the carrier distribution in our simulation to reveal the physical situation behind these results. Fig. 5.5.4 shows the calculated carrier distribution in these UV LEDs structure under a high forward current density of 100 A/cm^2 (1000 mA). When we adjust the band-offset ratio and increase the carrier mobility in InGaN/InAlGaN MQWs, the carrier distribution becomes uniform. Comparing to electrons, hole distribution shows more non-uniform due to holes have larger effective mass and lower mobility. Thus, the adjustment in hole mobility and band-offset ratio can reduce the carrier leakage and increase the chance of electron-hole pair radiatively recombination.

Table 5.1 Simulation parameters in band-offset ratio and carrier mobility

| | Band offset ratio | Electron mobility ($\text{cm}^2/\text{V}^{-1}\text{s}^{-1}$) | Hole mobility ($\text{cm}^2/\text{V}^{-1}\text{s}^{-1}$) |
|--------------------|-------------------|--|--|
| InGaN/AlGaN MQWs | 6 : 4 | 354 | 2 |
| InGaN/InAlGaN MQWs | 7 : 3 | 642 | 5 |

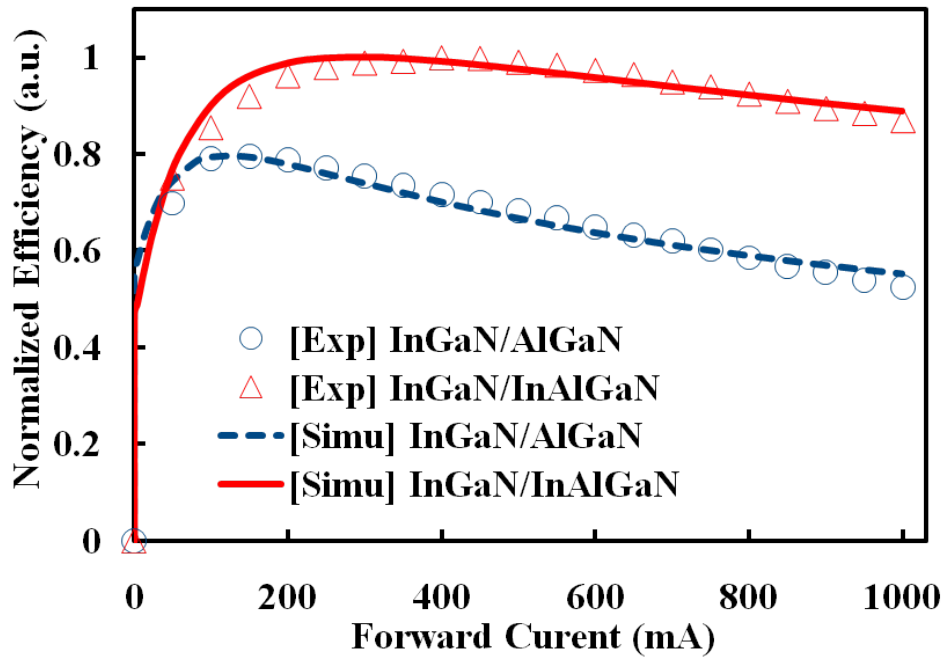


Fig. 5.5.3 Normalized Efficiency curves of experimental and simulated.

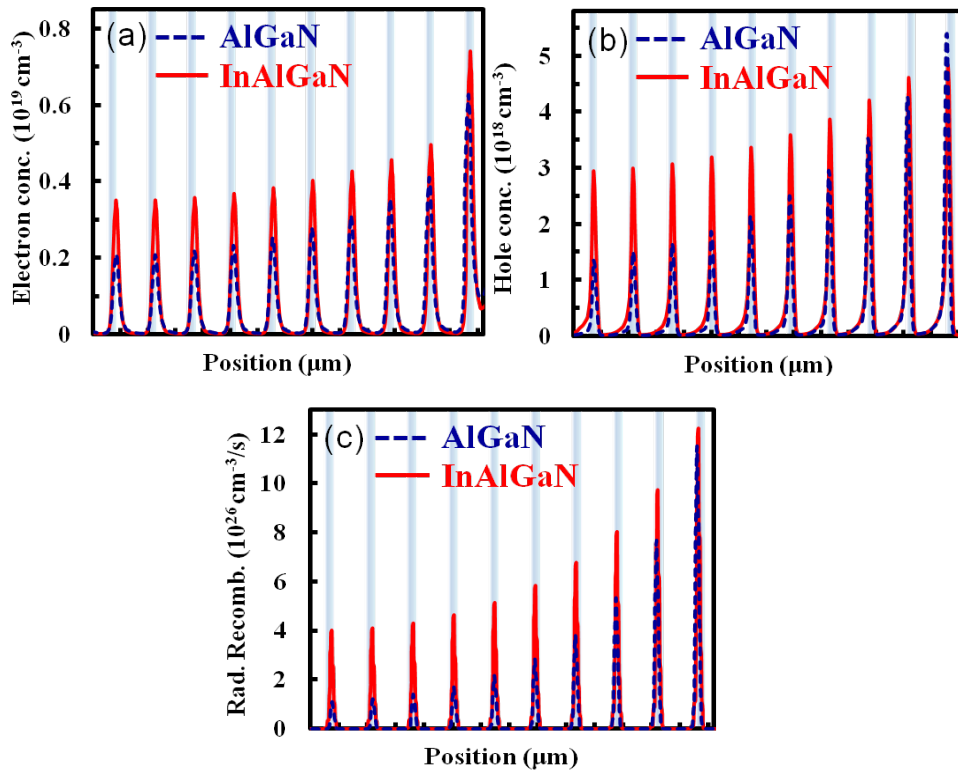


Fig. 5.5.4 Distribution of (a) Electron (b) Hole concentrations, and (c) Radiative recombination rates concentrations of the LEDs with AlGaN and InAlGaN barrier under a high forward current density of 100 A/cm^2 .

5.6 Summery

In summary, we have compared InGaN-based UV MQWs active region with ternary AlGaN and quaternary InAlGaN barrier layers. HRXRD and TEM measurements show the two barriers are consistent with the lattice, and smooth morphology of quaternary InAlGaN layer can be observed in AFM. Under a particular investigation, the electroluminescence results indicate that the light performance of the InGaN-based UV LEDs can be enhanced effectively when the conventional LT AlGaN barrier are replaced by the InAlGaN barrier. Furthermore, simulation results show that InGaN-based UV LEDs with quaternary InAlGaN barrier exhibit higher radiatively recombination rate and lower efficiency droop at a high injection current. We attribute this change to a drastic improvement in the light output and efficiency droop from the higher band-offset ratio and higher carrier mobility within quantum barriers, substantially higher hole mobility leads to the superior redistribution of holes and reduction of scatterings due to better morphology in the transverse carrier transport through the InGaN/InAlGaN MQWs.

Chapter 6 Conclusion

In this thesis, in order to improve hole transportation and reduce droop behavior, we first designed a graded-composition electron blocking layer (GEBL) with aluminum composition increasing along the (0001) direction for c-plane InGaN/GaN LEDs by employing the band-engineering. The simulation results demonstrated that such GEBL can effectively enhance the capability of hole transportation across the EBL as well as the electron confinement. After analyzing different graded range of aluminum composition by simulation, we chose the $\text{Al}_{0-0.25}\text{GaN}$ GEBL for utilization. Consequently, the LED with GEBL grown by MOCVD exhibited better electrical properties and much higher output power at high current density as compared to conventional LED. Meanwhile, the efficiency droop was reduced from 34% in conventional LED to only 4% from the maximum value at low injection current to 200 A/cm^2 .

Second, we demonstrated relatively lower efficiency droop in InGaN-based UV LEDs by with InAlGaN barriers compared to AlGaN barriers. Measurement results show the two barriers are consistent with the lattice and bandgap except the surface morphology. EL results indicate that the light output performance can be enhanced effectively when the conventional AlGaN barriers are replaced by the InAlGaN. Furthermore, from numerical analysis, we find InGaN-based UV LEDs with quaternary InAlGaN barrier have better band-offset ratio and the higher carrier mobility. It is believed that InGaN/InAlGaN MQWs exhibit higher radiative recombination rate and low efficiency droop at a high injection current because of the better band-offset ratio and the

higher carrier mobility leading to uniform distribution of holes in the active region.

These two works imply that with appropriately selecting the material and composition variation, the profiles of band-diagram in active region could be modified and so does the carrier transportation behavior. So the injection and transportation of holes could be enhancing. Our results also prove that improving hole transportation is very useful for alleviating efficiency droop.



Reference

- [1] <http://www.ecse.rpi.edu/~schubert/Light-Emitting-Diodes-dot-org>
- [2] T. G. Zhu, D. J. H. Lambert, B. S. Shelton, M. N. Wong, U. Chowdhury, H. K. Kwon, and R. D. Dupuis, *Electron Lett.*, **36**, 1971 (2000)
- [3] G. T. Dang, A. P. Zhang, F. Ren, X. A. Cao, S. J. Pearton, H. Cho, J. Han, J. I. Chyi, C. M. Lee, C. C. Chuo, S. N. G. Chu, and R. G. Wilson, *IEEE Trans. Electron Devices*, **47**, 692 (2000)
- [4] B. S. Shelton, D. J. H. Lambert, H. J. Jang, M. M. Wong, U. Chowdhury, Z. T. Gang, H. K. Kwon, Z. Liliental-Weber, M. Benarama, M. Feng, and R. D. Dupuis, *IEEE Trans. Electron Devices*, **48**, 490 (2001)
- [5] A. P. Zhang, J. Han, F. Ren, K. E. Waldrio, C. R. Abernathy, B. Luo, G. Dang, J. W. Johnson, K. P. Lee, and S. J. Pearton, *Electronchem. Solid-State Lett.*, **4**, G39 (2001)
- [6] J. I. Pankove, E. A. Miller, and J. E. Berkeyheiser, *J. Luminescence*, **5**, 84 (1992)
- [7] H. Amano, N. Sawaki, I. Akasaki, and Y. Toyoda, *Appl. Phys. Lett.*, **48**, 353 (1986)
- [8] H. Amano, N. Sawaki, I. Akasaki, and Y. Toyoda, *Jpn. J. Appl. Phys.*, **28**, L2112 (1989)
- [9] S. Nakamura, T. Mukai, M. Senoh, and N. Iwasa, *Jpn. J. Appl. Phys.*, **31**, 1258 (1992)
- [10] S. Nakamura, T. Mukai, M. Senoh, S. Nagahama, and N. Iwasa, *Journal of Applied Physics*, **74**, 3911 (1993)
- [11] K. J. Vampola, M. Iza, S. Keller, S. P. DenBaars, and S. Nakamura, *Appl. Phys. Lett.*, **94**, 061116 (2009)
- [12] Y. C. Shen, G. O. Muller, S. Watanabe, N. F. Gardner, A. Munkholm, and M. R. Krames, *Appl. Phys. Lett.*, **91**, 141101 (2007)
- [13] Y. Yang, X. A. Cao, and C. Yan, *IEEE Transactions On Electron Devices*, **55**, 1771 (2008).
- [14] B. Monemar and B. E. Sernelius, *Appl. Phys. Lett.* **91**, 181103 (2007).
- [15] M. H. Kim, M. F. Schubert, Q. Dai, J. K. Kim, E. F. Schubert, J. Piprek, Y. Park, *Appl. Phys. Lett.* **91**, 183507 (2007).
- [16] K. J. Vampola, M. Iza, S. Keller, S. P. DenBaars, and S. Nakamura, *Appl. Phys. Lett.* **94**, 061116 (2009)

- [17] K. Ding, Y. P. Zeng, X. C. Wei, Z. C. Li, J. X. Wang, H. X. Lu, P. P. Cong, X. Y. Yi, G. H. Wang, J. M. Li, *Appl Phys B*, **97**, 465–468 (2009).
- [18] C. H. Wang, J. R. Chen, C. H. Chiu, H. C. Kuo, Y. L. Li, T. C. Lu, and S. C. Wang, *IEEE Photon. Technol. Lett.* **22**, 236 (2010).
- [19] A. David and M. J. Grundmann, *Appl. Phys. Lett.* **96**, 103504 (2010).
- [20] B. Monemar and B. E. Sernelius, *Appl. Phys. Lett.* **91**, 181103 (2007).
- [21] M. F. Schubert, J. Xu, J. K. Kim, E. F. Schubert, M. H. Kim, S. Yoon, S. M. Lee, C. Sone, T. Sakong, and Y. Park, *Appl. Phys. Lett.* **93**, 041102 (2008).
- [22] Y. K. Kuo, J. Y. Chang, M. C. Tsai, and S. H. Yen, *Appl. Phys. Lett.* **95**, 011116 (2009).
- [23] R. A. Arif, Y. K. Ee, and N. Tansu, *Appl. Phys. Lett.* **91**, 091110 (2007).
- [24] S. C. Ling, T. C. Lu, S. P. Chang, J. R. Chen, H. C. Kuo, and S. C. Wang, *Appl. Phys. Lett.* **96**, 231101 (2010).
- [25] J. Xie, X. Ni, Q. Fan, R. Shimada, Ü. Özgür, and H. Morkoç, *Appl. Phys. Lett.* **93**, 121107 (2008).
- [26] W. Götz, N. M. Johnson, C. Chen, H. Liu, C. Kuo, and W. Imler, *Appl. Phys. Lett.* **68**, 3144 (1996).
- [27] V. Bougrov, M. E. Levinshtein, S. L. Rumyantsev, and A. Zubrilov, in *Properties of Advanced Semiconductor Materials: GaN, AlN, InN, BN, SiC, SiGe*, edited by M. E. Levinshtein, S. L. Rumyantsev, and M. S. Shur Wiley, New York, 2001, pp. 1–30.
- [28] U. Kaufmann, P. Schlotter, H. Obloh, K. Köhler, and M. Maier, *Phys. Rev. B* **62**, 10867 (2000).
- [29] M. Farahmand *et al.* *IEEE Trans. Electron Devices*, **48**, 535 (2001)
- [30] A. David, M. J. Grundmann, J. F. Kaeding, N. F. Gardner, T. G. Mihopoulos, and M. R. Krames, *Appl. Phys. Lett.* **92**, 053502 (2008).
- [31] M.-H. Kim, M. F. Schubert, Q. Dai, J. K. Kim, E. Fred Schubert, J. Piprek, and Y. Park, *Appl. Phys. Lett.* **91**, 183507 (2007).
- [32] S.-H. Han, D.-Y. Lee, S.-J. Lee, C.-Y. Cho, M.-K. Kwon, S. P. Lee, D. Y. Noh, D.-J. Kim, Y. C. Kim, and S.-J. Park, *Appl. Phys. Lett.* **94**, 231123 (2009).
- [33] S. Choi, H. J. Kim, S.-S. Kim, J. Liu, J. Kim, J.-H. Ryou, R. D. Dupuis, A. M. Fischer, and F. A. Ponce, *Appl. Phys. Lett.* **96**, 221105 (2010).

- [34] Y. K. Kuo, M. C. Tsai, and S. H. Yen, *Opt. Commun.* **282**, 4252 (2009).
- [35] S. L. Chuang and C. S. Chang, *Phys. Rev. B*, vol. 54, pp. 2491–2504, (1996).
- [36] I. Vurgaftman and J. R. Meyer, *J. Appl. Phys.*, vol. 94, pp. 3675–3691, (2003).
- [37] Y. P. Varshni, *Physica*, vol. 34, pp. 149-154 (1967)
- [38] Osamura, K., Naka, S., and Murakami, Y., *J. Appl. Phys.* 46, (1975), 3432.
- [39] M. E. Aumer, S. F. LeBoeuf, F. G. McIntosh, and S. M. Bedair, *Appl. Phys. Lett.*, vol. 75, pp. 3315–3317, (1999).
- [40] C. G. Van de Walle and J. Neugebauer, *Nature*, vol.423, pp. 626–628, 2003.
- [41] V. Fiorentini, F. Bernardini, and O. Ambacher, *Appl. Phys. Lett.*, vol. 80, pp. 1204–1206, (2002).
- [42] J. P. Ibbetson, P. T. Fini, K. D. Ness, S. P. DenBaars, J. S. Speck, and U. K. Mishra, *Appl. Phys. Lett.*, vol. 77, pp. 250–252, (2000).
- [43] S. F. Chichibu, A. C. Abare, M. S. Minsky, S. Keller, S. B. Fleischer, J. E. Bowers, E. Hu, U. K. Mishra, L. A. Coldren, S. P. DenBaars, and T. Sota, *Appl. Phys. Lett.*, vol. 73, pp. 2006–2008, (1998).
- [44] C. M. Caughey and R. E. Thomas, *Proc. IEEE*, vol. 55, no. 12, pp. 2192–2193, (1967).
- [45] C. K. Sun, T. L. Chiu, S. Keller, G. Wang, M. S. Minsky, S. P. DenBaars, and J. E. Bowers, *Appl. Phys. Lett.* **71**, 425 (1997).
- [46] M.-H. Kim, Y.-G. Do, H. C. Kang, D. Y. Noh, and S.-J. Park, *Appl. Phys. Lett.* **79**, 2713 (2001).
- [47] J. Simon, V. Protasenko, C. Lian, H. Xing, and D. Jena, *Science* **327**, 60 (2010).
- [48] A. Sandhu, *Nature Photonics* **1**, 38 (2007).
- [49] Y. S. Tang, S. F. Hu, C. C. Lin, N. C. Bagkar, and R. S. Liu, *Appl. Phys. Lett.* **90**, 151108 (2007).
- [50] Y. C. Chiu, W. R. Liu, C. K. Chang, C. C. Liao, Y. T. Yeh, S. M. Jang, and T. M. Chen, *J. Mater. Chem.* **20**, 1755 (2010).
- [51] H. Hirayama, *J. Appl. Phys.* **97**, 091101 (2005).
- [52] I. H. Ho and G. B. Stringfellow, *Appl. Phys. Lett.* **69**, 2701 (1996).
- [53] T. Mukai and S. Nakamura, *Jpn. J. Appl. Phys.* **38**, 5735 (1999).

- [54] R. H. Horng, W. K. Wang, S. C. Huang, S. Y. Huang, S. H. Lin, C. F. Lin, and D. S. Wu, *J. Cryst. Growth* **298**, 219 (2007).
- [55] D. Morita, M. Yamamoto, K. Akaishi, K. Matoba, K. Yasutomo, Y. Kasai, M. Sano, S. i. Nagahama and T. Mukai, *Jpn. J. Appl. Phys.* **43**, 5945 (2004).
- [56] A. Knauer, H. Wenzel, T. Kolbe, S. Einfeldt, M. Weyers, M. Kneissl, and G. Tränkle, *Appl. Phys. Lett.* **92**, 191912 (2008).
- [57] J. Zhang, J. Yang, G. Simin, M. Shatalov, M. A. Khan, M. S. Shur, and R. Gaska, *Appl. Phys. Lett.* **77**, 2668 (2000).
- [58] J. J. Wu, G. Y. Zhang, X. L. Liu, Q. S. Zhu, Z. G. Wang, Q. J. Jia, and L. P. Guo, *Nanotechnology* **18**, 015402 (2007).
- [59] S. H. Baek, J. O. Kim, M. K. Kwon, I. K. Park, S. I. Na, J. Y. Kim, B. J. Kim, S. J. Park, *IEEE Photonics Technology Lett.* **18**, 1276 (2006).
- [60] S. Suihkonen, O. Svensk, P. T. Törmä, M. Ali, M. Sopanen, H. Lipsanen, M. A. Odnoblyudo and V. E. Bougrov, *J. Cryst. Growth* **301**, 1777 (2008).
- [61] M. Asif Khan, J.W. Yang, G. Simin, R. Gaska, M.S. Shur, H.-C. zur Loye, G. Tamulaitis, A. Zukauskas, *Appl. Phys. Lett.* **76** (2000) 1161.
- [62] J. J. Wu, X. X. Han, J. M. Li, H. Y. Wei, G. W. Cong, X. L. Liu, Q. S. Zhu, Z. G. Wang, Q. J. Jia, L. P. Guo, T. D. Hu and H. H. Wang, *Optical Materials* **28**, 1227 (2006).
- [63] M. H Kim, M. F. Schubert, Q. Dai, J. K. Kim, E. F. Schubert, J. Piprek, and Y. Park, *Appl. Phys. Lett.* **91**, 183507 (2007).
- [64] C. G. Van de Walle and J. Neugebauer, *Nature*, vol.423, pp. 626–628, (2003).